Additive Manufacturing 30 (2019) 100835

Contents lists available at ScienceDirect

Additive Manufacturing

journal homepage: www.elsevier.com/locate/addma

Full Length Article

Keyhole-induced porosities in Laser-based Powder Bed Fusion (L-PBF) of Ti6Al4V: High-fidelity modelling and experimental validation

Mohamad Bayat[a,*], Aditi Thanki[b], Sankhya Mohanty[a], Ann Witvrouw[b], Shoufeng Yang[b], Jesper Thorborg[a], Niels Skat Tiedje[a], Jesper Henri Hattel[a]

[a] Department of Mechanical Engineering, Technical University of Denmark, building 425, Lyngby, Denmark
[b] KU Leuven, Department of Mechanical Engineering – Member of Flanders Make, Celestijnenlaan 300, 3001, Heverlee, Belgium

ARTICLE INFO

Keywords:
Multiphysics model
The L-PBF process
Keyhole formation
Porosity
Multiple reflection
X-CT analysis

ABSTRACT

Metal additive manufacturing, despite of offering unique capabilities e.g. unlimited design freedom, short manufacturing time, etc., suffers from raft of intrinsic defects. Porosity is of the defects which can badly deteriorate a part's performance. In this respect, enabling one to observe and predict the porosity during this process is of high importance. To this end, in this work a combined numerical and experimental approach has been used to analyze the formation, evolution and disappearance of keyhole and keyhole-induced porosities along with their initiating mechanisms, during single track L-PBF of a Ti6Al4V alloy. In this respect, a high-fidelity numerical model based on the Finite Volume Method (FVM) and accomplished in the commercial software Flow-3D is developed. The model accounts for the major physics taking place during the laser-scanning step of the L-PBF process. To better simulate the actual laser-material interaction, multiple reflection with the ray-tracing method has been implemented along with the Fresnel absorption function. The results show that during the keyhole regime, the heating rises dramatically compared to the shallow-depth melt pool regime due to the large entrapment of laser rays in the keyhole cavities. Also a detailed parametric study is performed to investigate the effect of input power on thermal absorptivity, heat transfer and melt pool anatomy. Furthermore, an X-ray Computed Tomography (X-CT) analysis is carried out to visualize the pores formed during the L-PBF process. It is shown, that the predicted shape, size and depth of the pores are in very good agreement with those found by either X-CT or optical and 3D digital microscopic images.

1. Introduction

Metal Additive Manufacturing (MAM) is a production method where the components are made layer by layer. Laser-based Powder Bed Fusion (L-PBF) is a branch of the MAM in which lasers are used as heating sources for fusing the material together [1].

In the L-PBF process, initially the building platform moves a small increment down in the z-direction (a typical machine for the process is shown in Fig. 1). Then the coating tool evenly spreads a layer of fine spherical particles, stored in the neighboring powder container, on the building platform. Right after this powder-feeding step, the laser starts scanning predefined locations provided by the component's CAD file [2–4]. The amount of laser heat input is typically so high that it can easily melt down the powder particles and fuse them together. As the scanning step is finished, the building table moves another increment down along the z-direction and this chain of steps is repeated until the whole component is manufactured.

The L-PBF process is considered to be a superior manufacturing process because of its capability of producing complex designs, its low material waste and its short total manufacturing time. Although L-PBF outweighs some other manufacturing processes e.g. casting, milling, etc., in a number of aspects, the components made by means of this method still suffer from a major number of defects which are detrimental to the part's mechanical strength [5–7]. These defects cover a wide range, spanning from voids [8] and internal porosities to cracks [9], delamination and large deformations [10]. Voids or internal porosities in L-PBF might occur under two completely different conditions of insufficient [8,11] and excessive heat input [12]. More specifically, the former condition leads to lack-of-fusion voids while the latter leads to keyhole-induced pores.

One way of detecting these types of porosities is via either *ex-situ* [13] or *in-situ* [14] investigations. The *ex-situ* investigations would give insufficient information about how the pores are formed and as such will not reveal the mechanisms from which these voids are made. Also

* Corresponding author.
E-mail address: mbayat@mek.dtu.dk (M. Bayat).

https://doi.org/10.1016/j.addma.2019.100835
Received 3 April 2019; Received in revised form 10 July 2019; Accepted 16 August 2019
Available online 17 August 2019

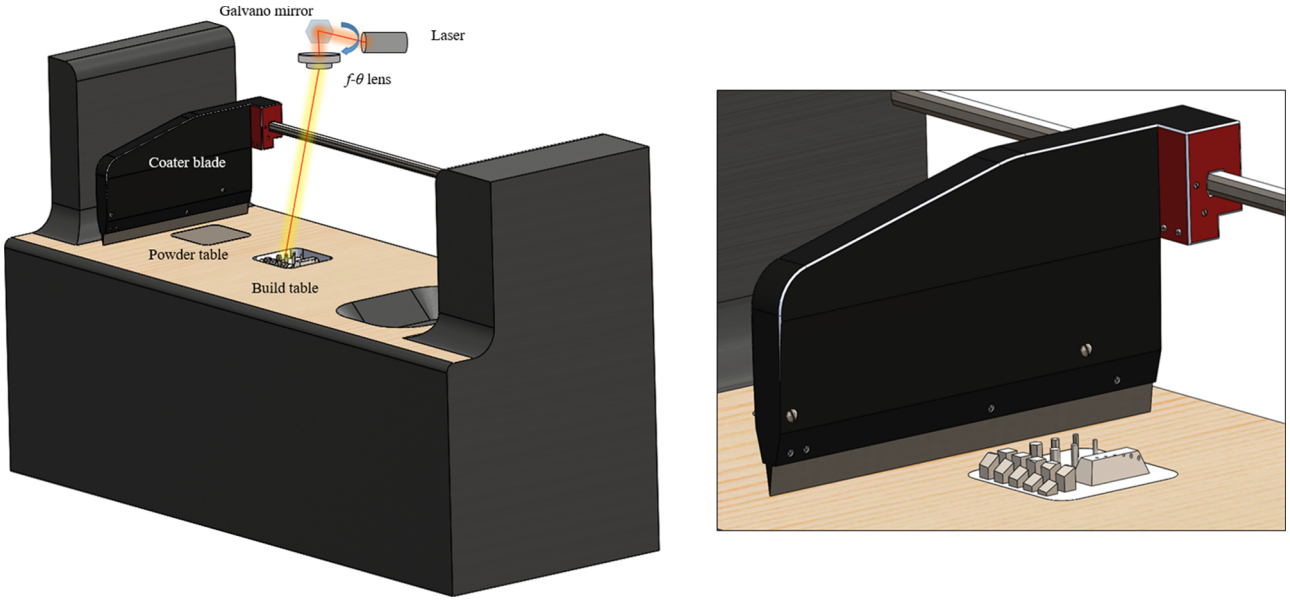

Fig. 1. 3D view of a typical L-PBF machine. The laser is guided through an *f-θ* lens and a Galvano mirror. To the right the final shape of the sample is shown. The coater transfers the remaining powder to the right container.

in-situ monitoring systems are often very expensive and can also constitute health problems for operators [15] and in this way cannot be used frequently for observation of these types of physical phenomena. Moreover, online monitoring requires a series of sophisticated preparations and calibrations, a priori [14,16], which in turn increases the total analysis time considerably. Also these online methods often lead to huge amount of output data which can be difficult to both process and store. Furthermore, the coexistence of various interactive phenomena e.g. recoil pressure, capillary forces, Marangoni effect, evaporation, laser reflection, etc., all happening within microns and micro seconds, makes it extremely difficult to study the keyhole and its subsequent pore formation mechanism, solely by means of experiments.

An alternative way, however, could be using a calibrated numerical model that can capture most of the involved physics of the process. In this respect, high fidelity numerical models with the inclusion of fluid flow and free surface-tracking have been recently used to predict the shape of the melt pool along with its free surface [7]. These models, when validated with experimental results, will give invaluable information about the final quality of the samples and in this way they can be used as a cheap, smart and reliable tool for understanding the mechanisms of defect formation.

For instance, Khairallah and Anderson made a high-resolution numerical model (based on the ALE3D multiphysics code from Lawrence Livermore National Laboratory) of an L-PBF process of 316 L stainless steel to investigate the effect of surface tension on the melt pool morphology in which they managed to model the Plateau-Rayleigh instability as well [17]. However, since their model neglected the physics of recoil pressure, Marangoni effect and radiation, they had to keep the energy density as low as possible, in order not to get into the keyhole mode condition. This strategy of simplified fluid flow has also been adopted by other researchers like Shrestha and Chou accounting for only the surface tension in their calculations [18]. The exclusion of the mentioned physics will highly reduce the heat transfer, leading to long melt pool tails which cause an overestimation of the solidification time [19]. As a result, Khairallah et al. further developed their numerical model and included the Marangoni effect along with the recoil pressure [20]. In this work, they investigated the evolution of the melt pool during L-PBF, in detail. Lee and Zhang developed a finite volume (FVM) model for analyzing both the melt pool geometry and the grain morphology [21] of a dual-track L-PBF process. They included multiple reflection to better simulate the laser-material interaction. However, the melt pool regime was still in the stable shallow-depth mode due to relatively low heat input. Qiu et al. investigated the effect of laser scanning speed on the porosity levels with a FVM model [22]. In their calculations, they only focused on high laser speeds leading to shallow melt pools as well. Leitz et al. studied the effect of different powder characteristics on the melt pool shape based on a finite element (FEM) framework [23]. Matthews et al. also developed an FEM-based model of L-PBF to study the effect of different process conditions on the denudation of powder [24] during the process. Finally, Wu et al., made a more fundamental investigation in which they studied the effect of inclusion or exclusion of evaporation on the melt pool profile for a single-track L-PBF process [25]. Bayat et al. also went one step further and modelled the evolution of lack-of-fusion voids during a multi-track multi-later L-PBF process [26]. It is noteworthy to emphasize that all of the above mentioned numerical models, which are currently the state-of-the-art, despite of being applied to different process conditions and metals, have been used to study L-PBF processes involving shallow-depth melt pool regimes, only.

Interestingly, there has been a wide range of contributions in studying the keyhole mode and its subsequent pore formation in both L-PBF and laser welding processes with high heat input [12,27–32]. As stated by Panwisawas et al. [29], the mechanisms of keyhole and keyhole-induced porosities require further research, since they are still not very well known. There are various justifications proposed for keyhole pore formation in the literature. For instance, according to [29], the main reason for pore formation in a keyhole regime is said to be instabilities and periodic collapse of keyhole walls. King et al. [12] mentioned that under certain conditions, the depression regime transforms to a keyhole. They managed to identify the necessary conditions for keyhole formation for a stainless steel via an analytical expression along with a vast number of experimental results [12]. Choquet et al. [30] stated that it is vortices, recirculations and high fluid speeds which cause pore formation and their entrapment in a keyhole regime. Or as found by Martin et al. [31], through a combined *in-situ* observation and numerical simulation, the keyhole porosities are trapped when the Marangoni force outweighs the buoyancy effect (not clarified which type of buoyancy, either thermal or density). In another recent work, Cunningham et al. [32] captured the keyhole evolution and its porosity formation with an ultrahigh-speed X-ray imaging system for a wide range of process conditions of a titanium alloy. However, despite of observing the phenomena in great spatiotemporal detail, they did not

give any information regarding how and why pores and keyhole were formed – leaving behind the physical interpretations and justifications. In contrast to the pure experimental works of King et al. [12] (*ex-situ*) and Cunningham et al., [32] (*in-situ*), Tang et al. [28] studied the keyhole formation with a high-fidelity model for a L-PBF of a stainless steel. Their work, however, did not include any experimental investigation and the keyhole-induced porosities were qualitatively compared with welding and L-PBF results in the literature.

In this respect, although there has been deep studies on the monitoring or simulation of keyhole formation, there has not been any potential investigation on how and why exactly the keyhole and keyhole porosities are formed in L-PBF, with the focus on the role of laser-material interactions.

In view of this, we have implemented a combined numerical and experimental approach to investigate the formation and evolution of keyhole-induced porosities during the single-track L-PBF process of a Ti6Al4V alloy. The high-fidelity numerical model accomplished in the commercial software Flow-3D is based on FVM and includes recoil pressure, evaporation and evaporative cooling, two phase flow, Marangoni effect and capillary forces. Moreover, to make the model even more accurate, multiple reflection along with Fresnel absorption are used as well [33]. The powder layer distribution is found via a discrete element method (DEM) calculation also in Flow-3D, similar to that of Lee and Zhang [21]. Also a detailed and systematic parametric study is carried out to investigate the effect of input laser power on absorptivity, heat and fluid flow conditions. Furthermore, experimental investigations of parts built with the L-PBF process are conducted. More specifically, different line scans were made on top of the bulk domain, which clearly lead to keyhole porosities. The scan tracks were studied via X-CT analysis along with optical microscopic images. The size, shape, depth and distribution of the porosities predicted by the model were found to be in very good agreement with those of the conducted experiments. Moreover, the predicted melt pool's top profile was also very close to the one observed by the 3D digital microscope.

2. Model description and experimental setup

2.1. Governing equations

The computational domain consists of two immiscible phases of gas and metal, knowing that the metal itself undergoes another phase change during melting and solidification. Equations of continuity and momentum transport are solved for the metallic phase to find the coupled fields of velocity and pressure, i.e. [34]:

$$\vec{\nabla}\cdot(\vec{V}) = 0 \tag{1}$$

$$\rho\left[\frac{\partial}{\partial t}(\vec{V}) + \vec{V}\cdot\vec{\nabla}(\vec{V})\right] = -\vec{\nabla}P + \vec{\nabla}\cdot\left[\mu\left(\vec{\nabla}\vec{V} + \vec{\nabla}\vec{V}^{T} - \frac{2}{3}\vec{\nabla}\cdot\vec{V}\right)\right] - \frac{K_C(1-f_l)^2}{C_K + f_l^3}\vec{V} - \rho\vec{g}\beta(T - T_l), \tag{2}$$

where V (m/s) and p (Pa) are the velocity vector and pressure field, respectively. The second term on the right hand side of Eq. (2) represents the forces caused by viscous stresses and the third term is the solidification drag force due to the formation of a mushy zone [7,35]. The last term in Eq. (2) accounts for the buoyancy effect. In this work the flow is assumed to be incompressible and hence to model the buoyancy force, the Boussinesq approximation has been used where β (1/K) stands for the thermal expansion coefficient in Eq. (2) [19]. K_C (kg/(m^3 s)) and C_K (-) are the constants used for solidification drag forces and they are typically in the order of 10^6 and 10^{-4}, respectively. The energy transport equation is solved and coupled to the momentum transport equation to obtain the corresponding temperature field during the L-PBF process, i.e.:

$$\rho\left[\frac{\partial}{\partial t}(h) + \vec{V}\cdot\vec{\nabla}(h)\right] = \vec{\nabla}\cdot[k_{bulk}(\vec{\nabla}T)], \tag{3}$$

$$h = h_{ref} + C_{p,bulk}(T - T_{ref}) + f_l\Delta H_{sl}, \tag{4}$$

$$f_l = \begin{cases} 0 & T < T_s \\ \dfrac{T - T_s}{T_l - T_s}, & T_s \le T \le T_l \\ 1 & T_l < T \end{cases} \tag{5}$$

where h (kJ/kg) is the specific enthalpy of the metallic phase and the subscript O_{ref} stands for the reference state from which the enthalpy is evaluated. f_l (-) is the liquid fraction function defined in Eq. (5), which for simplicity is approximated by a linear function of temperature and ΔH_{sl} (kJ/kg) in Eq. (4) is the latent heat of fusion. Finally, the material properties of the mushy zone, such as density, thermal conductivity and specific heat capacity are approximated by a linear weight-averaged method, i.e. [36]:

$$\rho = f_s\rho_s + f_l\rho_l \tag{6}$$

$$k_{bulk} = f_s k_s + f_l k_l \tag{7}$$

$$C_{p,bulk} = \frac{f_s\rho_s C_{p,s} + f_l\rho_l C_{p,l}}{f_s\rho_s + f_l\rho_l}. \tag{8}$$

Volume of fluid (VOF) advection with the split Lagrangian method is used to track and determine the exposed surfaces of the metallic phase, i.e.:

$$\frac{\partial}{\partial t}(F) + \vec{\nabla}\cdot(F\vec{V}) = 0, \tag{9}$$

where the scalar F (-) equals zero and unity inside the gaseous and metallic phases, respectively [37]. Intermediate values of F indicate an interface between these two immiscible phases.

2.2. Triple forces and laser model

As earlier mentioned, there are three major forces acting on the surface of a liquid metal which can highly deform its free surface [26]

$$P_{recoil} = 0.54\left[P_0\exp\left(\frac{\Delta H_{lv}}{R_v\cdot T_{boil}}\left(1 - \frac{T_{boil}}{T}\right)\right)\right], \tag{10}$$

$$\tau_{Marangoni} = \gamma[\vec{\nabla}T - \vec{n}(\vec{\nabla}T.\ \vec{n})], \tag{11}$$

$$P_{capillary} = (\sigma_0 + \gamma[T - T_l])\kappa. \tag{12}$$

Eq. (10) expresses the recoil pressure that causes depression of the melt pool, when the temperature exceeds the evaporation point T_{boil} (K) (at the atmospheric pressure of P_O (Pa)) [33] and R_v (J/kg/K) is the vapor metal gas constant. Eqs. (11) and (12), respectively, show the tangential and normal tractions caused by Marangoni and capillary effects. The surface tension in Eq. (12) is assumed to be a linear function of temperature. κ (1/m) is the curvature of the exposed metallic surface and γ (N/m/K) is the sensitivity of the surface tension to temperature.

For modelling the laser-material interaction, multiple reflection is implemented where it is assumed that the reflecting laser ray will depart the free surface of the metallic phase according to a simple mirror law, i.e. [38,39]

$$\vec{I}_{i,j+1} = \vec{I}_{i,j} - 2(\vec{I}_{i,j}\cdot\vec{n}_{i,j})\vec{n}_{i,j}. \tag{13}$$

Where $n_{i,j}$ is the vector normal to the free surface of the metallic phase and vector I is the incident/reflected ray direction in Eq. (13). The subscripts i and j are respectively, ray identity and reflection index. The latter increases with every collision with the metallic phase surface until the amount of ray energy attenuates to less than 1% of its initial value, after which it disappears.

Furthermore, the exposed surface of the metallic phase transfers

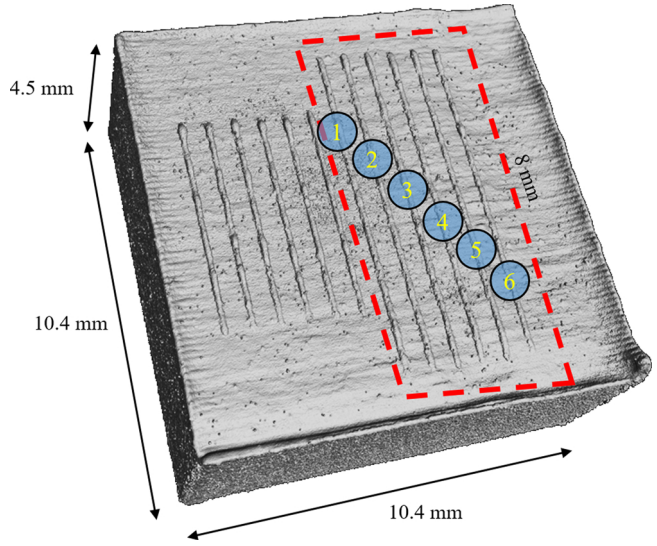

Fig. 2. Sample for experimental analysis produced by the KU Leuven in-house made L-PBF machine. The bulk size is 10.4 mm by 10.4 mm by 4.5 mm. Six scan tracks resulting in the keyhole mode with porosity are made with a length of 8 mm each.

heat to the surrounding and ambient via radiation and convection, while receiving individual ray heat fluxes according to the following equations

$$-k_{bulk}\frac{\partial T}{\partial n} = h(T - T_{surr}) + \in\sigma(T^4 - T_{surr}^4) - q''_{ij,laser} + q''_{evap}, \quad (14)$$

$$q''_{laser} = q_{max}\exp\left(-2\bullet\frac{r^2}{r_b^2}\right), \quad (15)$$

$$q''_{laser} = \sum_{i=1}^{n_r}\sum_{j=1}^{n_c} q''_{ij,laser}\bullet\alpha_{FR,ij}, \quad (16)$$

$$\alpha_{FR}(\varepsilon,\theta) = 1 - \frac{1}{2}\left(\frac{1+(1-\varepsilon\cos\theta)^2}{1+(1+\varepsilon\cos\theta)^2} + \frac{\varepsilon^2 - 2\varepsilon\cos\theta + 2\cos^2\theta}{\varepsilon^2 + 2\varepsilon\cos\theta + 2\cos^2\theta}\right), \quad (17)$$

$$q'^{'}_{evap} = \frac{0.01}{\sqrt{2\pi R_v T}}\cdot[P_0\ \exp(\frac{\Delta H_{lv}}{R_v\cdot T_{boil}}(1 - \frac{T_{boil}}{T}))]\cdot\Delta H_{lv}. \quad (18)$$

The thermal boundary condition for the exposed surface is expressed in Eq. (14). In this work it is assumed that the laser heat flux has a 2D Gaussian profile. r_b (m) is the effective radius of the beam where the heat flux is $1/e^2$ of its maximum value. According to Eq. (16), the total amount of the input energy transferred by every individual ray, must equal the total laser input energy [39]. n_c and n_r are the total number of rays and the total number of reflections, respectively. α_{FR} (-) in Eq. (17) is the Fresnel absorptivity which is a function of the individual ray incident angle with respect to normal to the surface (θ) and a material constant related to the electrical conductance [33,39]. The evaporative cooling is approximated by Eq. (18), based on the Clausius-Clapeyron empirical equation, where ΔH_{lv} (kJ/kg) stands for latent heat of evaporation.

2.3. Experimental details

Six line tracks were made on a bulk material of Ti6Al4V with a layer of 30 μm powder particles on top, with an in-house L-PBF machine developed by KU Leuven [40]. The machine works with a fiber laser with a wavelength of 1080 nm and a maximum output power of 1 kW. The bulk material's dimension is 10.4 mm by 10.4 mm by 4.5 mm as shown in Fig. 2 and it is built with a bi-directional scanning strategy.

X-CT analysis was carried out using a Nikon XT H 225 ST machine. The machine's maximum tube potential is 225 kV and the measurement settings were fixed at 180 kV, 12.1 W with an exposure time of 2000 ms and 3600 radiographs. The voxel sizes are 10 μm for the current X-CT analysis. Finally, the volume reconstruction was carried out based on the Feldkamp-Davis-Kress (FDK) algorithm.

2.4. Model details, boundary conditions and machine data

A discrete element calculation in the Flow-3D DEM-module was made to find the distribution of the powder particles during the powder-laying step [7]. The final shape of the computational domain with surface reconstruction along with the imposed boundary conditions are shown in Fig. 3.

The top part of the domain is empty while the rest is filled with the metallic phase. The bottom boundary is set to be adiabatic and the sides are slip-wall conditions. The x–z plane is a symmetry boundary and the top boundary has constant pressure and temperature (ambient temperature) where the material can escape if necessary [26]. The laser starts to scan the domain starting from point S all the way towards point F as seen in Fig. 3. 6,288,368 cells with an average size of 3.3 μm with an aspect ratio of very close to one have been used, which is ideal for surface tracking algorithms such as VOF. Processing conditions along with the used Ti6Al4V material properties are given in Table 1. The calculation time for this problem is 145 h on a 14-core machine with Intel Core i9-7940X 3.1 GHz CPU and 128 GB RAM.

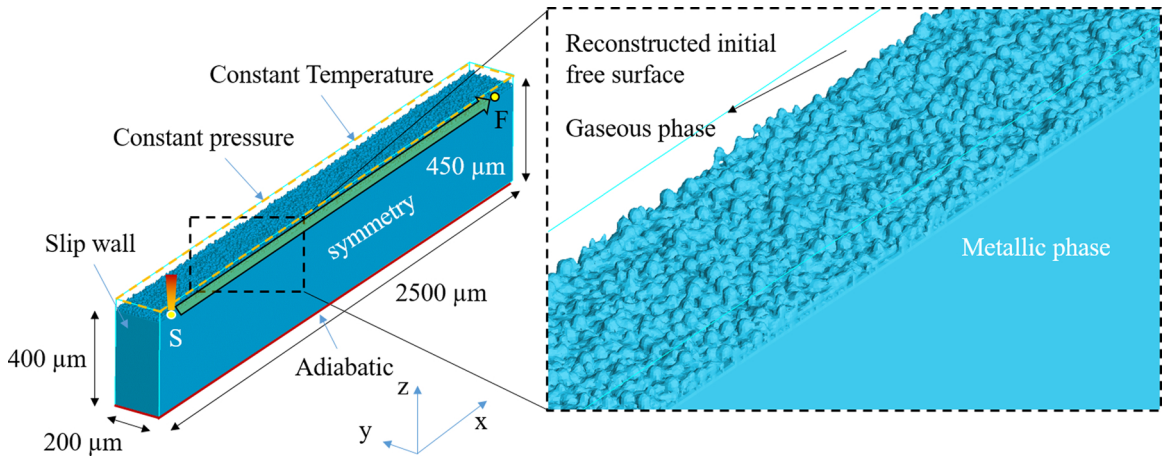

Fig. 3. 3D view of the whole computational domain. The control volume shown in cyan blue contains both metallic and gaseous phases. To the right a close-up view of the reconstructed free surface of the domain is shown.

Table 1
Ti6Al4V thermophysical properties and the L-PBF machine processing conditions for the single track tests [41–43].

Property	Value	Property	Value
Laser power	170 W	T_s	1878 K
Scanning speed	500 mm/s	T_l	1928 K
r_b $(1/e^2)$	25 μm	$C_{p,s}$	573 J/kg/K
σ_0	1.5 N/m	$C_{p,l}$	750 J/kg/K
γ	−0.00026 N/m/K	k_s	13 W/m/K
ΔH_{sl}	286 kJ/kg	k_l	33 W/m/K
ΔH_{lv}	9.7 MJ/kg	T_{boil}	3315 K
ρ	4400 kg/m^3	μ	0.005 Pa.s
h	25 W/m^2/K	ε	0.2
R_v	195 J/kg/K	β	0.000025 1/K
∈	0.4	T_{surr}	300 K

3. Results and discussion

3.1. Melt pool evolution: transition to keyhole mode

The temperature contour and the melt pool border along with the velocity vectors are all shown in Fig. 4 at four different times at the initial phase of the process. According to Fig. 4(a), the temperature right below where the laser irradiates, reaches a value above 3000 K while the surrounding powder layer is still at its initial temperature of 300 K. Due to the presence of air between the powder particles and also because of the relatively low particle-particle contact areas, the thermal resistance is significant, hence lowering the speed of transverse heat waves coming from the laser. This implies that the bulk material conducts heat much faster than the powder bed [11]. In Fig. 4(b) it is seen that a relatively big depression is formed at the location of the previously formed hot zone and below the laser. This depression is largely due to the presence of a significant recoil pressure and to a smaller extent [20], because of the Marangoni-induced flow. According to Eq. (10), the recoil pressure increases with temperature exponentially and accordingly, this will lead to an even deeper penetration as seen in Fig. 4(c).

When the keyhole has sufficiently penetrated downwards (inside the iso-lines), it will continue its way to the back of the melt, due to the high deformability of the liquid. At this moment where laser rays are either mostly unable to penetrate that far or have lost most of their energy due to a large number of collisions, the local temperature at the tail of the keyhole decreases. This low-temperature zone will lead to a local increase in the surface tension and a dramatic reduction in the recoil pressure in that location which eventually leads to the formation of a pore, according to Fig. 4(d).

To elucidate this rapid transition from shallow-depth melt pool to the keyhole condition, 2D and 3D temperature contours along with velocity vectors are depicted for three different times in Fig. 5.

According to Fig. 5(a) and (b), the melt pool is shallow and the depression zone is very small, a result of lower local temperature. Although the Marangoni effect is present here, this downwards movement is mainly governed by the prevalence of a strong recoil pressure acting on the top surface. Also a neatly-shaped clock-wise circulation is observed at the back of the melt pool in Fig. 5(a) and (b), which is typical for either L-PBF [27,28] or welding processes [38,44,45] involving high heat input. Interestingly, it is the coexistence of both strong downwards flow and the hotspot that leads to the formation and the subsequent growth of the keyhole. When the hotspot is formed below the depression zone (as a consequence of laser ray collisions), the strong

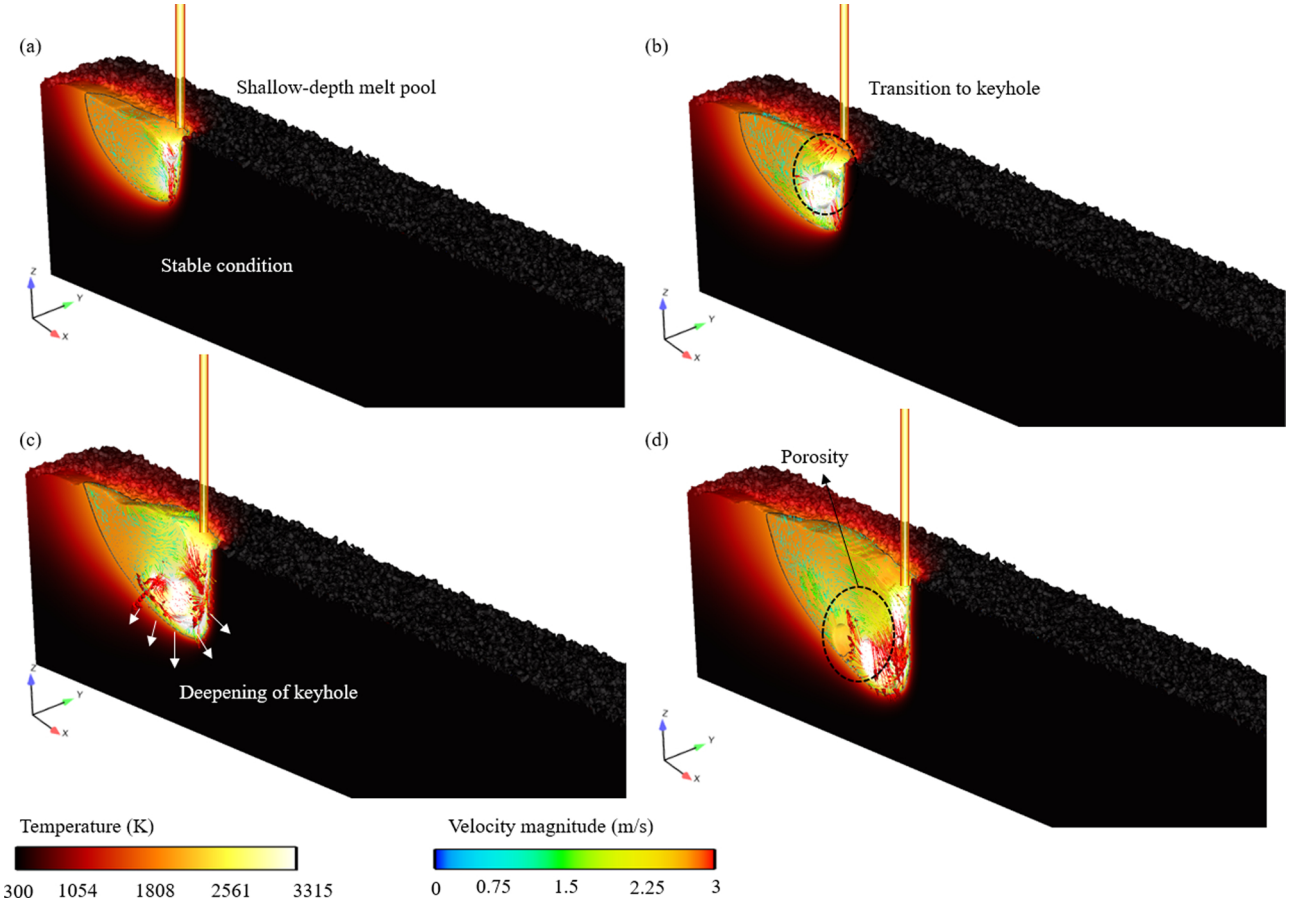

Fig. 4. Contour of temperature field along with fusion iso-lines and velocity vectors. (a) t = 0.695 ms, (b) t = 0.795 ms, (c) t = 0.995 ms and (d) t = 1.3 ms. Note the sudden transition from a stable melt pool to the unstable keyhole occurring from (a) to (b).

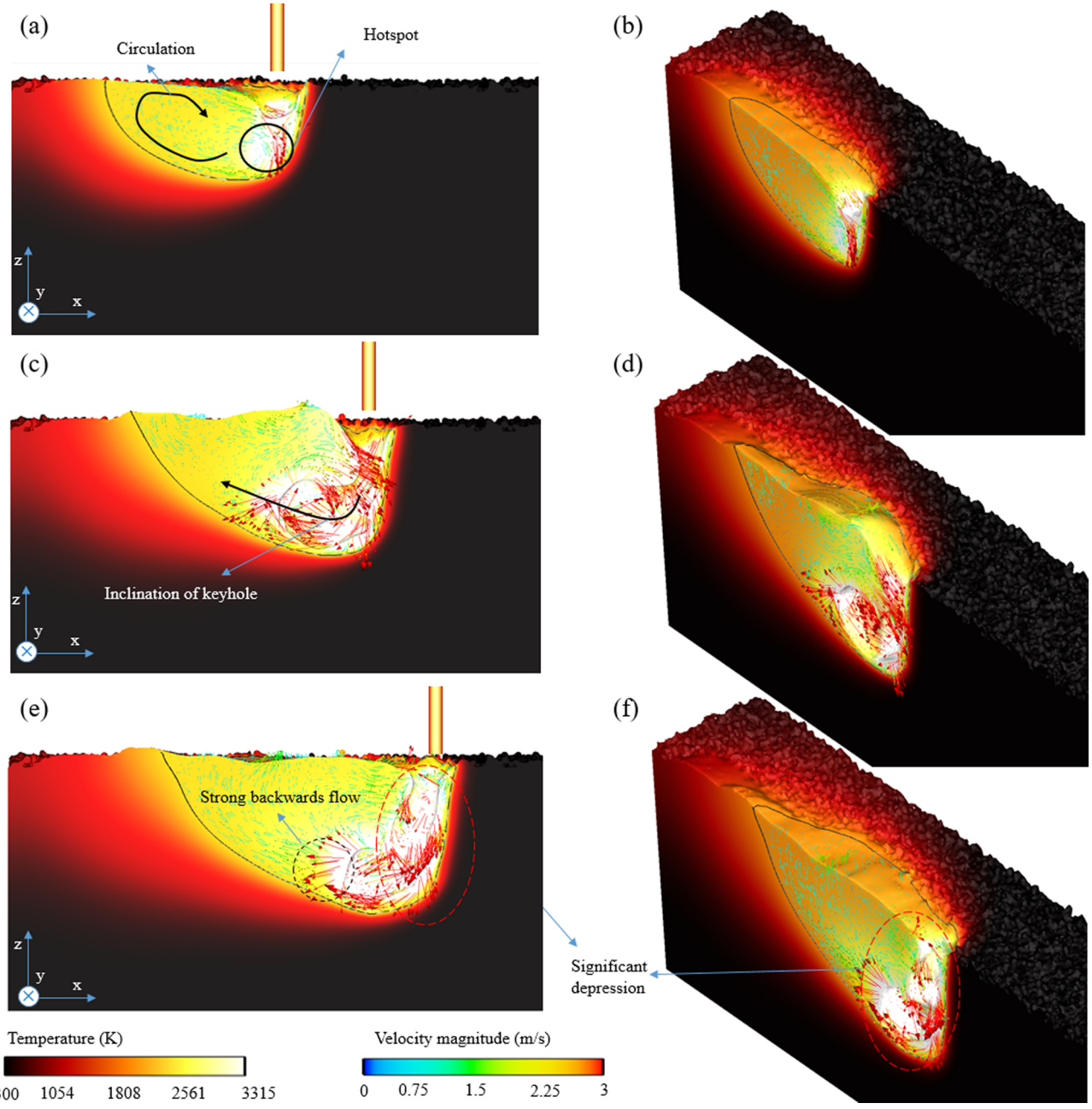

Fig. 5. Temperature contour and velocity field along with the melt pool borders for (a) t = 0.705 ms, (c) t = 1 ms and (e) t = 1.2 ms. (b), (d) and (f) are the corresponding 3D views.

downward flow will advect all the heat stored at this location along with the streamlines and to the back of the melt pool, according to Fig. 5(c) and (d). This advection of hot metal will in turn transfer heat further down and back into the melt pool, increasing the temperature of the regions close to the keyhole rims, leading to higher recoil pressure. Consequently, because of the exponential growth of the recoil pressure with respect to the temperature [25], the keyhole will incline further down and back into the melt pool as well. The same trend in transition from shallow to keyhole depression regime was reported in a recent study, involving ultrahigh-speed x-ray imaging, for a stationary laser illumination [32].

Once the keyhole is formed, the exposed surface area of the metallic phase which is in contact with the laser rays will increase dramatically. Consequently, more energy will be absorbed by the metallic phase which boosts the heat transfer to a large extent. As reported by Martin et al. [31], the reflections on the front of the depressions will cause vaporization on its rear. Moreover, one can visually compare the size of exposed surface area of the shallow-depth and keyhole melt pools in Fig. 5(a) and (e). In the stable condition, the exposed surface is much smaller than the one in the keyhole condition, according to Fig. 5. A larger exposed surface area of the metallic phase with complex shapes (like formation of a cavity or inclination of the keyhole backwards) has the potential to absorb even higher amounts of reflections, due to ray-entrainment. According to Fig. 6(a), in the shallow-depth condition, most of the rays will depart from the free surface of the metal with very few reflections, since the depression zone is shallow and there is no obstacle on the way for the reflecting rays.

In contrast to the stable melt pool in Fig. 6(a), when the keyhole is

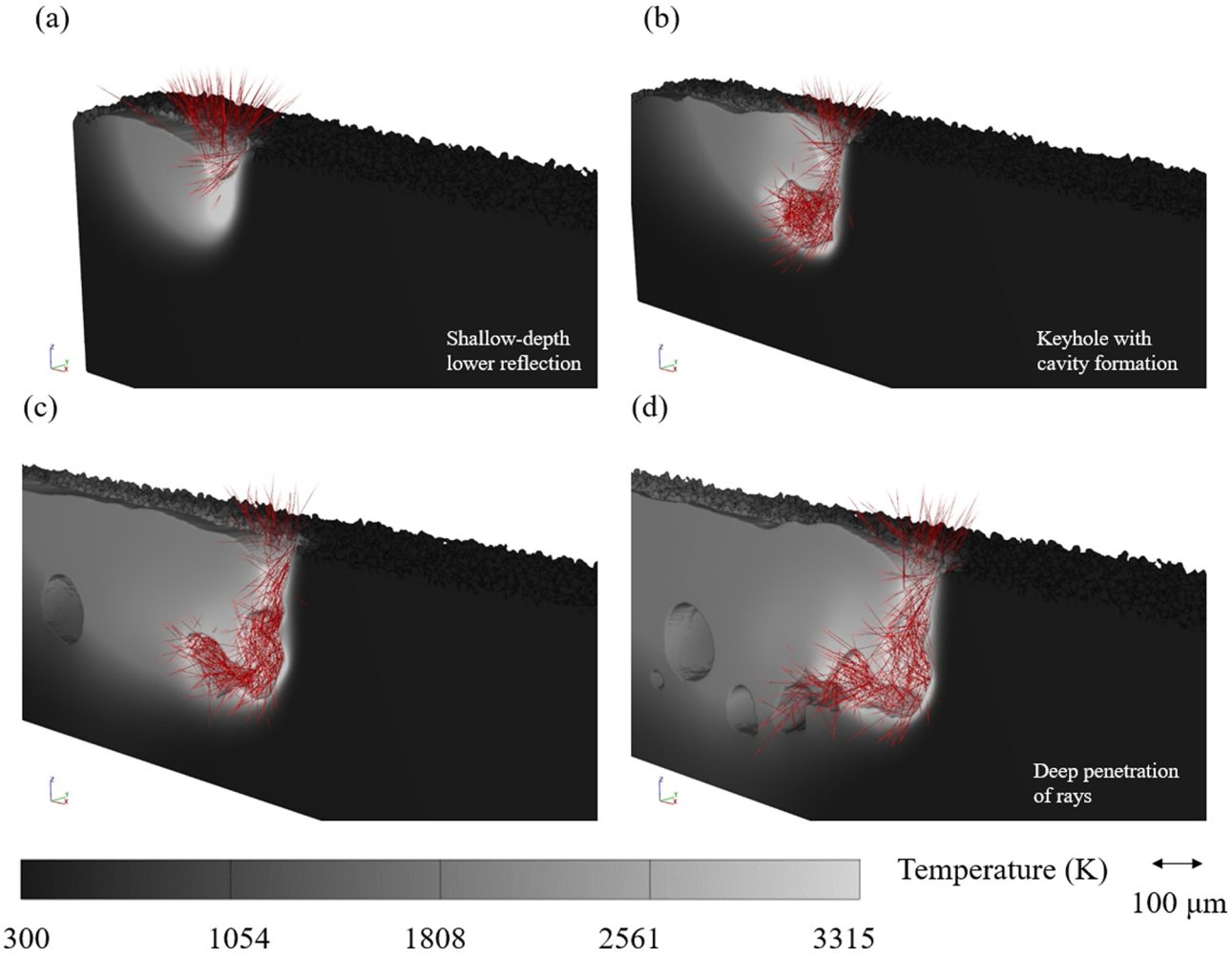

Fig. 6. Temperature contours along with the reflected laser ray trajectories departing the free surface of the metallic phase: (a) t = 0.6 ms, (b) t = 1 ms, (c) t = 2 ms and (d) t = 3 ms. A significant number of rays are trapped due to complex keyhole shapes in (b)–(d).

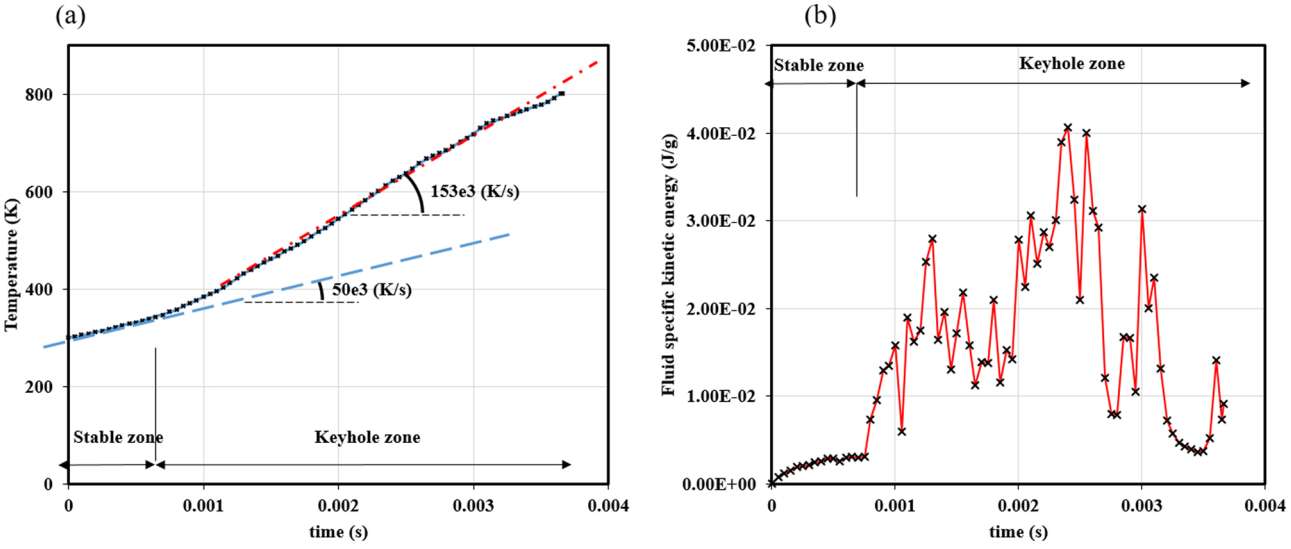

Fig. 7. Plots of (a) average metal temperature and (b) specific fluid kinetic energy versus time. Note the sudden change of heating rate in plot (a) after the keyhole has formed.

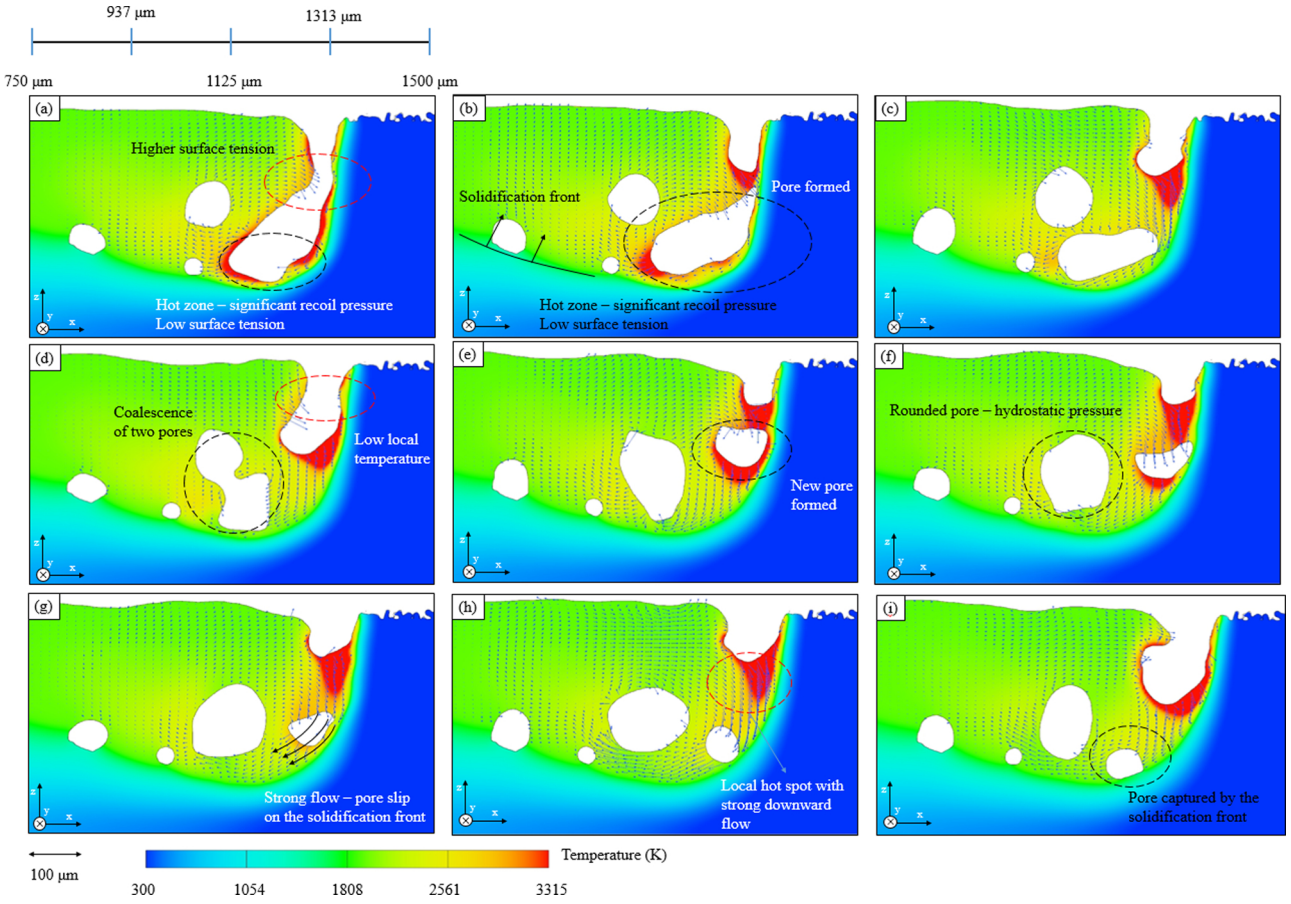

Fig. 8. Temperature contour and velocity field during formation of pores. (a) t = 2.395 ms, (b) t = 2.4 ms, (c) t = 2.415 ms, (d) t = 2.43 ms, (e) t = 2.445 ms, (f) t = 2.45 ms, (g) t = 2.455, (h) t = 2.47 ms and (i) t = 2.495 ms.

formed and subsequently has moved backwards, a large amount of rays get trapped in the cavities (Fig. 6(b)–(d)) in which situation they have to transfer a significant portion of their energy to the metal.

In this way, the formation of the keyhole is like a chain-process, where firstly the hole becomes relatively deep, leading to a higher contact area of the metallic phase. Choquet et al. [30] also reported this keyhole interface undulations due to various forces e.g. recoil pressure because of strong temperature variation. Subsequently, by taking complex shapes, the keyhole will trap a large number of rays and absorb a lot of heat via multiple reflections. This will lead to stronger fluid flow and higher temperatures, which in turn will spread the hot liquid and enlarge the keyhole area. This is also supported by the plot of the average temperature of the metallic phase versus time shown in Fig. 7(a).

Trend lines of the average metal temperature are shown for the two different regions in Fig. 7(a) versus time. According to this figure, before the formation of the keyhole, the average heating rate is about 50,000 K/s whereas around t = 1 ms, the heating rate increases to about 153,000 K/s, mainly due to the formation of the keyhole and the resulting large ray-entrainments. It is worth noting that at the same time of the transition, the specific kinetic energy of the liquid metal undergoes a sharp change, see Fig. 7(b). These severe fluctuations of the depression's surface and depth noticed in Fig. 7(b) were also reported for keyhole welding processes as well [46,47]. This figure not only shows the significant increase of fluid motion, but also demonstrates how unstable the keyhole regime is [29,30]. This pronounced increase in the fluid flow motion along with higher energy absorption because of increased ray-entrainments, lead to better mixing of the hot metal liquid, improving the heat transfer in the melt pool to a very large extent. Zhao et al. [47] called these severe changes, self-fluctuations, for welding process in keyhole regime.

3.2. Porosity formation mechanism

As mentioned earlier, the keyhole represents a highly unstable regime [48]. This severe instability is one of the key factors in formation of porosities [29,30]. To better visualize the formation, evolution or disappearance of porosities, a 2D cross section of the x–z plane parallel to the laser path is shown in Fig. 8 at different times. According to Fig. 8(a), the bottom of the keyhole is heated above the evaporation point of Ti6Al4V, which leads to an exponential rise in local recoil pressure and at the same time a linear decrease in the surface tension that keeps the keyhole open at this point. However, the cold local zone in the upper region of the keyhole shown by the red dashed line will lead to the opposite phenomenon and hence an increase in the surface tension, see Fig. 8(a). This local cold zone will subsequently close and as shown in Fig. 8(b), lead to the appearance of a strangely-shaped pore. At the same time when the depression zone is hit by the rays, the recoil pressure increases again and a strong downwards flow forms below the depression zone which will transport the pore further back into the melt pool, see Fig. 8(c). Another important factor that leads to porosity in a keyhole condition is the formation of strong clock-wise flow at the rear part of the keyhole [38,44,45], shown in Figs. 5 and 8.

Interestingly, Martin et al. [31] also observed the transport of pores

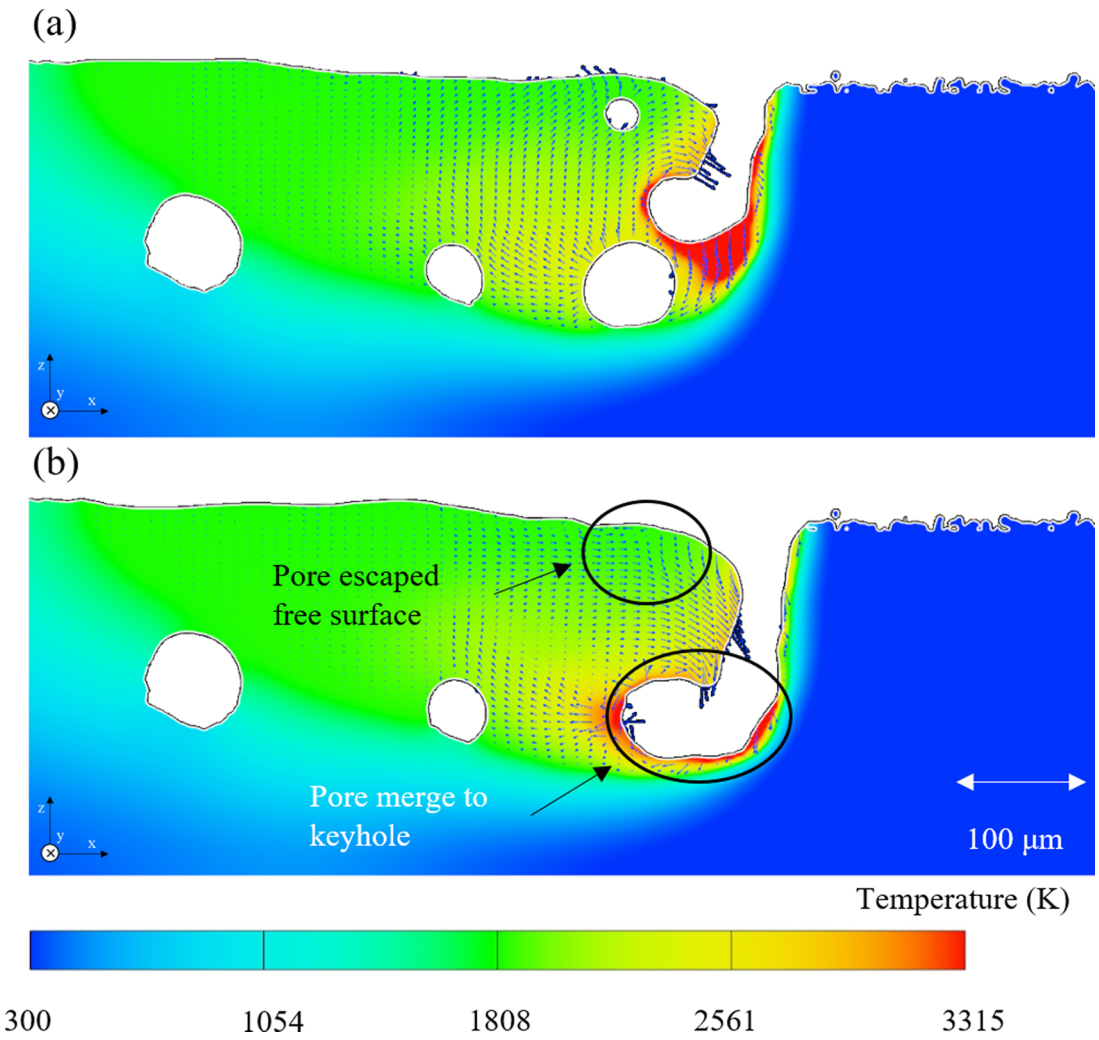

Fig. 9. Free surface along with temperature contour and velocity field at the central longitudinal plane at: (a) t = 2.205 ms and (b) t = 2.215 ms. Note the two mechanisms of which a pore can disappear.

along the streamlines via a high-speed x-ray imaging. When the pore has been transported further back into the melt pool, it coalesces with another pore formed previously, leading to another exotically-shaped pore, see Fig. 8(d). At the same time another local cold zone is formed indicated with the red dashed line in Fig. 8(d), paving the way for yet another pore formation as seen in Fig. 8(e). Due to the hydrostatic pressure of the liquid metal acting on all of sides of the pores, these will eventually become rounded see Fig. 8(f). This is in line with Martin et al. [31] who argued that this spheroidization is due to the fact that the surface tension tries to minimize the surface area. It is worth noting that, according to Fig. 8(a), the shape of the depression zone (keyhole) matches well with a recent online monitoring study done by Cunningham et al [32], where the toe of melt pool was inclined in the same pattern as in our model. As seen earlier, the hotspots formed below the depression zone in Fig. 8(f) and (g), will once more cause a pronounced recoil pressure and a subsequent strong downwards flow. Accordingly, the pore is transported to the back of the melt pool because of this strong flow of liquid metal. As indicated on Fig. 8(h), the recoil pressure will dominate the surface tension (which tries to keep the hole closed, minimizing the total surface energy) and this starts the keyhole's penetration towards the liquid metal in Fig. 8(h) and (i), while enlarging the open keyhole at the same time. It is worth to mention that the newly-formed pore because of its proximity to the fusion lines and the advancing solidification front, will be captured and remain there henceforth. The rapid-advancing solidification front is found to be one of the key factors for pore-entrapment, especially for materials such as aluminum [38,44]. Also it is worth to mention that the smaller pore seen in Fig. 8(a) has been shifted to the left in the mushy zone approximately 40 μm, Fig. 8(d), along the streamlines.

However, in several occasions the pores formed during the keyhole regime will escape or even disappear (due to merging with the keyhole). For instance there are two pores formed close to the depression zone, according to Fig. 9(a).

The smaller pore is close to the free surface and is located at the top left of the indentation zone, while the bigger pore is formed at the toe of the depression zone (see Fig. 9(a)). Then in Fig. 9(b) it is very well observed that the two pores seen in Fig. 9(a), are no longer existent. Moreover, the mechanisms of which these pores disappeared are different; the smaller pore escaped to the top free surface while the bigger one merged with the tail of the indentation. It is worth to note that this entire process of disappearance occurred within 10 μs, which highlights the rapid nature of the L-PBF process.

An example of formation and movement can be seen in Fig. 10(a) and (b–f), respectively.

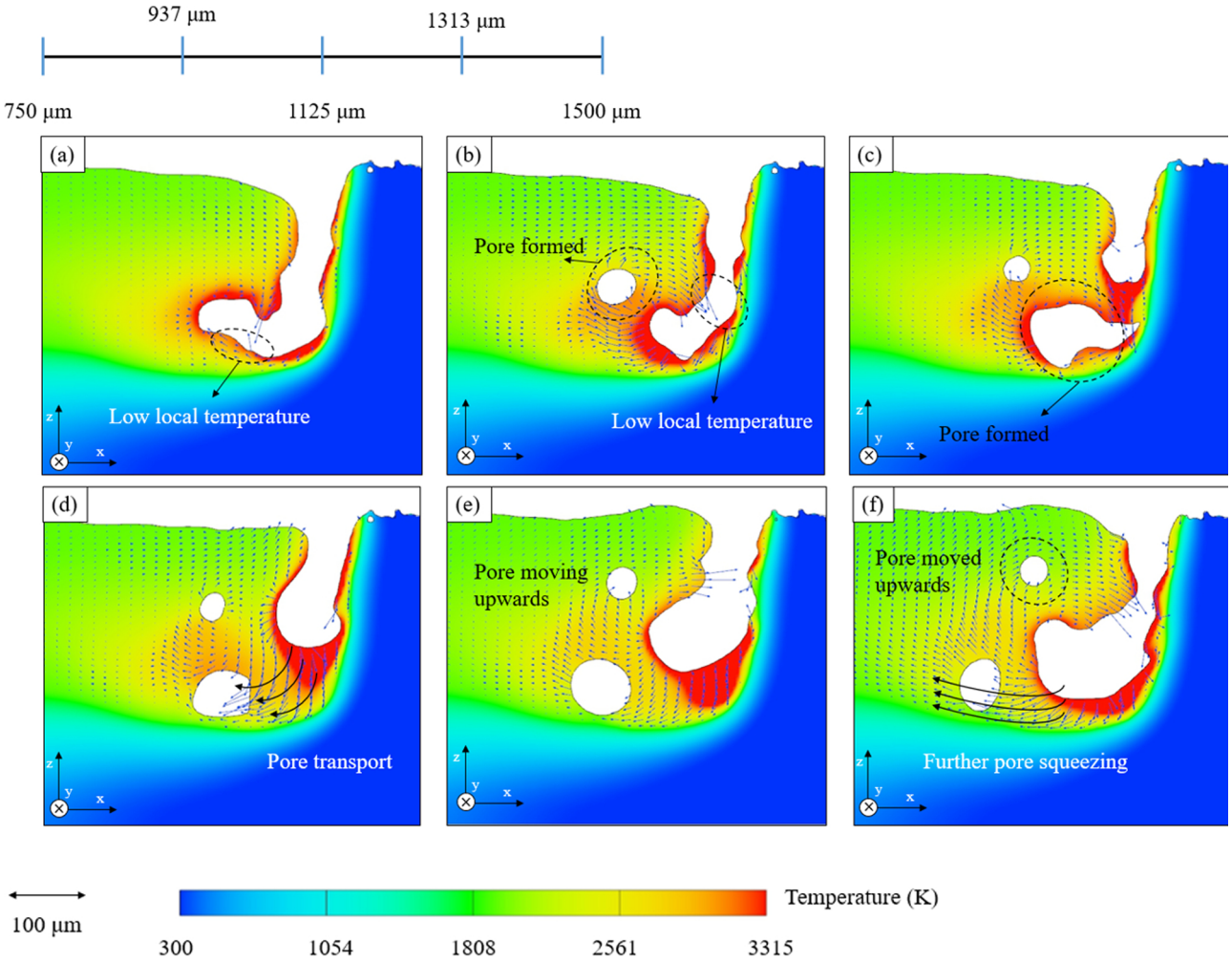

Fig. 10. Temperature contour and velocity field during formation of pores. (a) t = 2.05 ms, (b) t = 2.06 ms, (c) t = 2.065 ms, (d) t = 2.075 ms, (e) t = 2.09 ms and (f) t = 2.1 ms.

With the same mechanism, another pore is formed due to a local increase in the surface tension, in Fig. 10(c). Both of the pores are shifted towards left, largely because of the strong backwards recoil-induced flow. The smaller pore formed first is floating in the liquid metal and has a relatively small likelihood of getting trapped by the solidification front. By comparing Fig. 10(b) and (f), it is clear that this pore has moved upwards about 90 µm. Martin et al. [31] stated that the buoyancy effect has a negligible role in pore-entrapment. However, according to Fig. 10, we note that the strong density-driven buoyancy forces affect both the pore escape as well as the entrapment. The bottom pore however, despite of being subject to even stronger density-driven buoyancy due to its larger size, is almost frozen at the rim of the melt pool because of its contact with the mushy zone. Although the pore can slip along the melt pool borders due to the recoil-induced flow, it cannot move upwards. Finally, it should be emphasized once more that the predicted morphology of the depression shown in Fig. 10, is comparable with the ones observed via *in-situ* imaging of Ti6Al4V [31,32].

3.3. Effect of input power on absorptivity and heat transfer

Although the occurrence of a keyhole regime for a melt pool might lead to an unwanted porosity in samples (which in turn would badly influence the mechanical properties), it is crucial to have a sufficient intra-layer adhesion and bonding between neighboring layers [49]. One way of obtaining different penetration depths during either laser welding or L-PBF would be via changing the input laser power. In this respect a detailed parametric study has been performed to study the effect of this parameter on melt pool morphology, heat and fluid flow conditions. In addition, the data acquired from the parametric study is used to investigate the effect of melt pool geometry on the enhancement of heat transfer and overall energy absorption during the keyhole regime.

Six different laser input powers ranging from 50 W to 200 W with an interval of 30 W are chosen for the mentioned parametric study, simply designated as P50 to P200, while all other laser specifications are the same as stated in Table 1. The corresponding melt pool geometry along with its velocity vectors are presented in Fig. 11(a)–(f).

According to Fig. 11(a), at 50 W the melt pool is in a stable condition and its corresponding depression zone formed next to the laser beam position is shallow. This shallow depression (also called indentation [49]) is due to the fact that at 50 W the temperature of the free surface would not go much beyond the material's boiling point and in this way the recoil pressure cannot outweigh the surface tension. For cases P80 and P110, it is seen that the melt pool is still in a stable condition and no sign of oscillation is observed, according to Fig. 11(b)–(c). In a stable condition, the melt pool will not change in

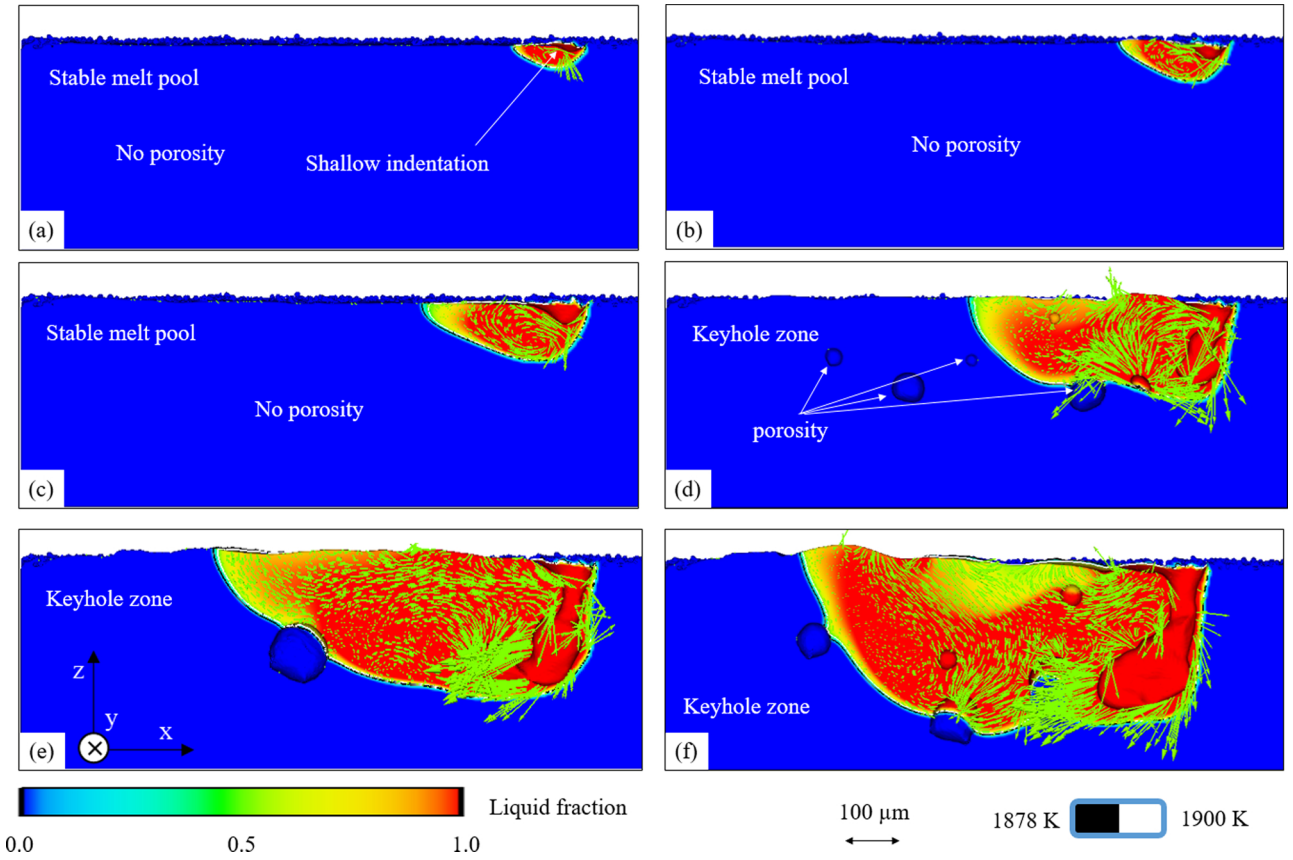

Fig. 11. Melt pool geometry and contour of liquid fraction along with velocity vectors for (a) P50, (b) P80, (c) P110, (d) P140, (e) P170 and (f) P200.

Table 2
Details of the melt pool condition and porosity for the parametric study.

	Melt pool data						Porosity data			
Case id	Depression (m)	Depth (m)	Volume (m^3)	Average velocity (m/s)	Pe (-)	Exposed surface (m^2)	Depth (m)	Diameter (m)	Porosity (-)	Frequency (1/s)
P50	1.25E-05	4.50E-05	5.16E-13	7.05E-01	4.70E+00	7.83E-07	–	–	–	–
P80	2.77E-05	6.62E-05	1.14E-12	7.40E-01	7.32E+00	7.72E-07	–	–	–	–
P110	4.18E-05	1.01E-04	2.52E-12	7.30E-01	1.07E+01	7.72E-07	–	–	–	–
P140	2.19E-04	2.53E-04	1.28E-11	9.31E-01	3.08E+01	8.47E-07	1.87E-04	5.76E-05	5.55E-02	3.33E+03
P170	2.95E-04	3.23E-04	2.07E-11	8.06E-01	3.40E+01	8.79E-07	2.53E-04	7.70E-05	7.48E-02	2.50E+03
P200	3.08E-04	3.45E-04	2.63E-11	1.08E+00	5.14E+01	9.35E-07	2.93E-04	1.03E-04	9.40E-02	2.22E+03

shape and size and will keep its morphology [19]. As there is no sign of oscillation or instability in cases P50, P80 and P110, no kind of porosity is formed and as a consequence, a dense morphology is predicted. Derived data regarding the melt pool behavior for all six cases are listed in Table 2.

However, according to Fig. 11(d), when the laser input power is set to 140 W, the melt pool enters an unstable keyhole regime with a much deeper indentation zone as compared to P110. There are several different features (compared to P110) seen in Fig. 11(d) belonging to case P140, e.g. stronger and more complex fluid flow involving more vortices, much bigger melt pool volume, deeper indentation zone and more importantly, formation of porosities. At 140 W and based on data provided in Table 2, although the laser power has been increased 27%, compared to P110, the increased heating lead to a melt pool which is approximately 5 times bigger in volume. This in essence highlights the increased heating due to the occurrence of the keyhole condition, which was also mentioned in the previous sections. One can notice that the linear relation between the melt pool's volume and input power seen in cases P50-P110, is no longer existent from P140 onwards. This is directly linked to the formation of the keyhole which leads to enhanced energy absorption due to more complex indentation shapes. Raising the input power to 170 W and subsequently to 200 W will result in an even deeper indentation and melt pool, as observed in Fig. 11(e) and (f). To analyze the relative importance of convective to conductive heat transfer, the Peclet number [19]:

$$Pe = \frac{\rho C_p U_b L_M}{k}, \tag{19}$$

is used. In Eq. (19) U_b (m/s) stands for average fluid velocity magnitude and L_M (m) expresses the melt pool's characteristic length [19]. A Peclet number larger than unity means that the convection is the dominant mode of heat transfer. Based on the data in Table 2, for all

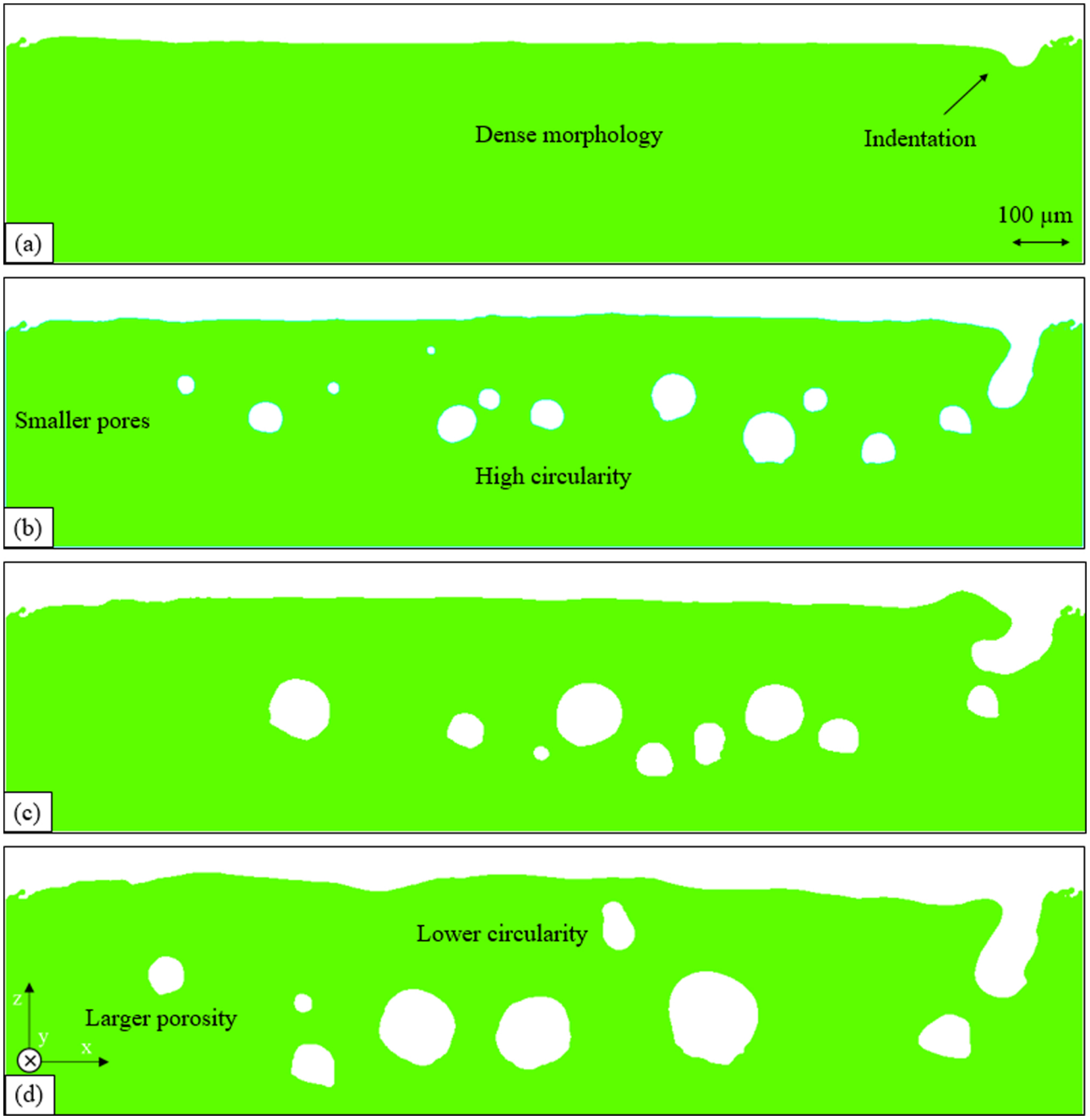

Fig. 12. Longitudinal view showing the free surface along with porosity distribution for cases: (a) P110, (b) P140, (c) P170 and (d) P200.

cases the Peclet number is substantially higher than unity – highlighting the importance of convection in heat transfer during this process. It is also noticed that the Peclet number will have a sharp jump as the laser power is raised from 110 W to 140 W, mainly due to the keyhole formation and better mixing.

Another set of data is provided in Table 2 which quantifies the depth, count and size of the porosities. As mentioned before, in this work, the porosity is only observed where the keyhole regime forms (except from the lack-of-fusion pores in multi-layer L-PBF [26]). According to Table 2, increasing the laser power will lead to bigger pore diameters with increasing depths. The longitudinal porosity profile and the fluid's free surface are demonstrated in Fig. 12(a)–(d) and at the end of the process.

As mentioned earlier, for P110 there is no sign of pore formation as the recoil pressure is insufficient to dominate the surface tension and hence a keyhole is avoided. Furthermore, there is a clear distinction between the pores formed in all three cases P140-P200, according to Fig. 12(b)–(d). In this figure it is observed that by increasing the laser power, both the pores' size and their depth from the top free surface are increased, which is also seen in Table 2. What might also be interesting is that, although both the porosity depth and the pores' average size increase with input power, the number of pores and hence their frequency of occurrence decreases. This can be due to the fact that at higher heat inputs, pores can merge together, as they have more time floating inside the larger liquid metal region.

To further investigate the overall effect of input laser power on heat

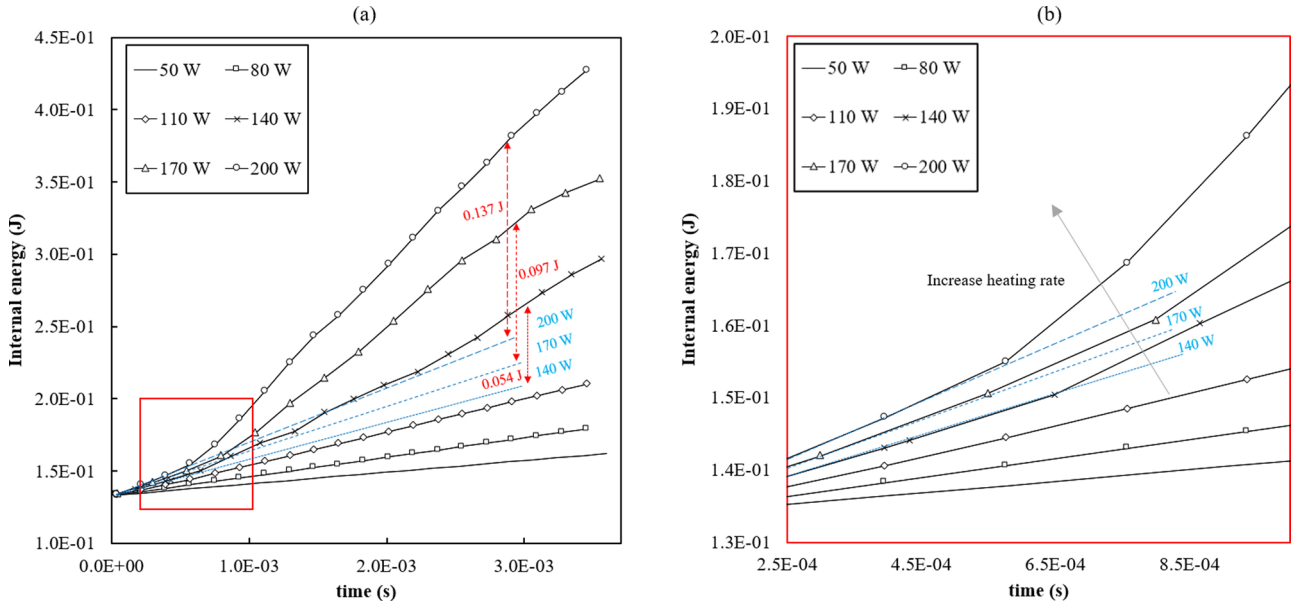

Fig. 13. (a) calculated total thermal energy of the domain versus time for all six cases. (b) the zoomed-in plot of (a) where melt pools are still at their corresponding stable conditions. Red arrows show the deviation in thermal energy level from their initial linear behavior. Blue dashed lines show the continuation of initial linear trends.

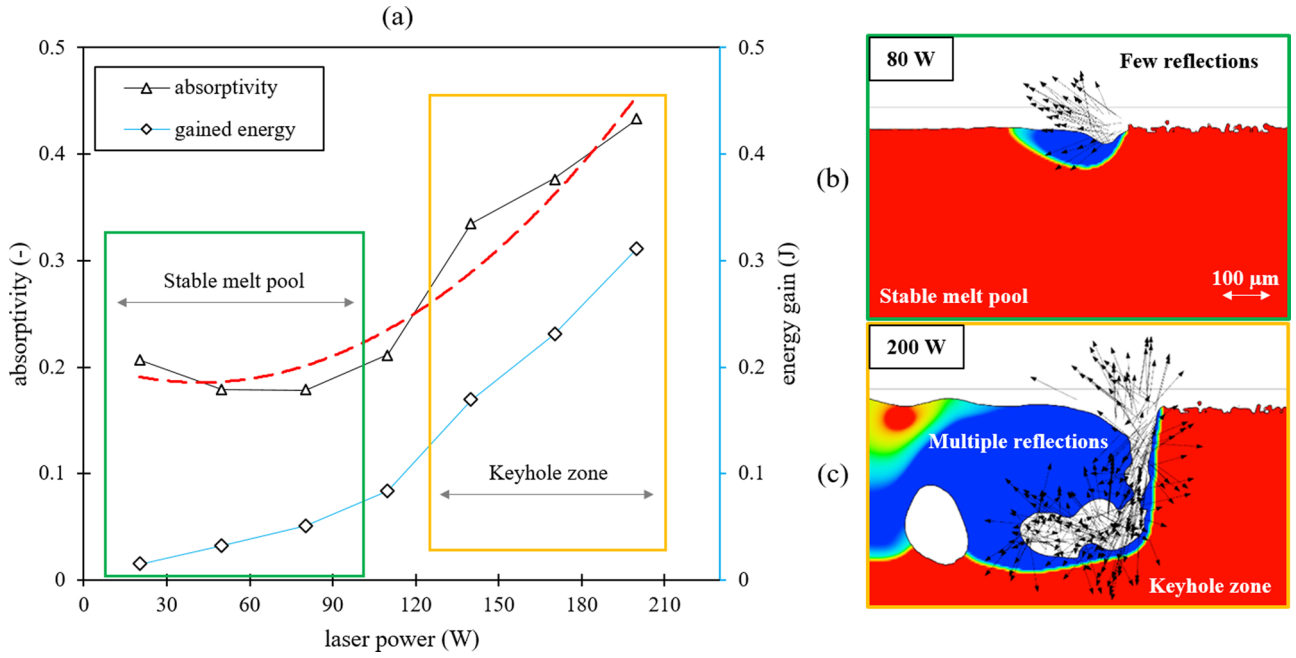

Fig. 14. (a) plot of nominal absorptivity and energy gain versus input laser power. (b) and (c) show melt pool morphology for P80 and P200 cases, respectively. Note that for P200 (yellow window), most of the rays are trapped because of the complex indentation configuration of the melt pool while for P80 (green window), most of the rays will depart the domain with very few collisions.

transfer during the L-PBF process of all six cases, the total thermal energy of the whole computational domain is calculated and plotted against time in Fig. 13(a) and (b).

According to Fig. 13(a) and (b), at laser powers of 50 W–110 W, where the melt pool is in a stable condition, the total thermal energy of the domain increases linearly with time, and as expected, higher energy levels are obtained for higher heat inputs accordingly. The curves will deviate from their initial linear trend as the input energy exceeds the threshold for keyhole formation, which in this study is found to be 140 W onwards. On the other hand, according to Fig. 13(b), it is observed that the curves' shape still follows a linear pattern at the very beginning of the process, where the melt pool is not fully evolved into the keyhole regime yet. The red dashed arrows shown in Fig. 13(a) show the deviation from the linear pattern for the domain's thermal energy and it is seen that further increase in the input power leads to even higher deviation, which is directly linked to the melt pool's

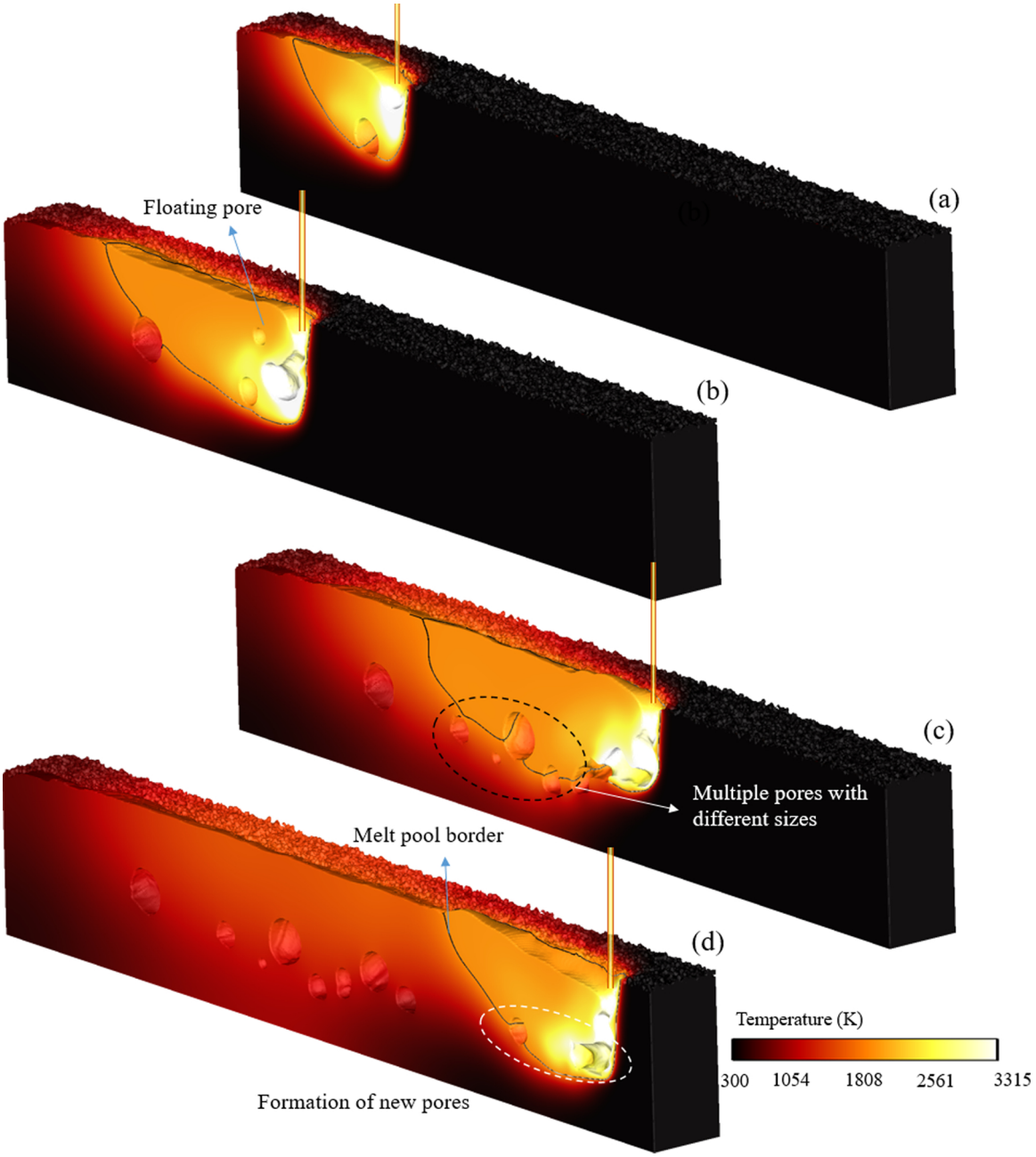

Fig. 15. Evolution of melt pool and formation of porosities: (a) t = 1.05 ms, (b) t = 2.095 ms, (c) t = 3 ms and (d) t = 4.5 ms.

geometry. To shed more light on this matter, the nominal absorptivity is determined for all six cases [50]:

$$\alpha_{nom} = \frac{\Delta E_{gain}}{\Delta E_{in}}, \tag{20}$$

$$\Delta E_{gain} = mC_p\Delta T_b, \tag{21}$$

$$\Delta E_{in} = P \bullet \Delta t_{contact}. \tag{22}$$

Where ΔE_{gain} (J) in Eqs. (20) and (21) is the gain in thermal energy of the domain calculated by means of the average domain temperature denoted T_b (K). ΔE_{in} (J) in Eq. (22) is the input energy from the laser and $\Delta t_{contact}$ (s) is the total laser-material contact time. The nominal absorptivity and gain in thermal energy of the domain are both determined and plotted against input laser power for all cases in Fig. 14(a).

Based on Fig. 14(a), at laser powers below 140 W, the absorptivity is almost unchanged, where earlier it was shown that the melt pool is in a stable condition. In this case and as shown in Fig. 14(b), most of the laser rays will depart the free surface of the domain with very few collisions and this will lead to a low nominal absorptivity according to Fig. 14(a). However, a steep change is seen in the α_{nom}-P curve for laser powers in the range of 110 W–140 W, which is due to the formation of a keyhole. As shown in Fig. 14(c), when a keyhole is formed, most of the rays will get trapped in complex keyhole configurations and in this way be forced to transfer most of their energy to the domain – boosting the heat transfer and nominal absorptivity. A similar trend in α_{nom}-P was also observed for L-PBF via an experimental investigation carried out by Trapp et al. [50].

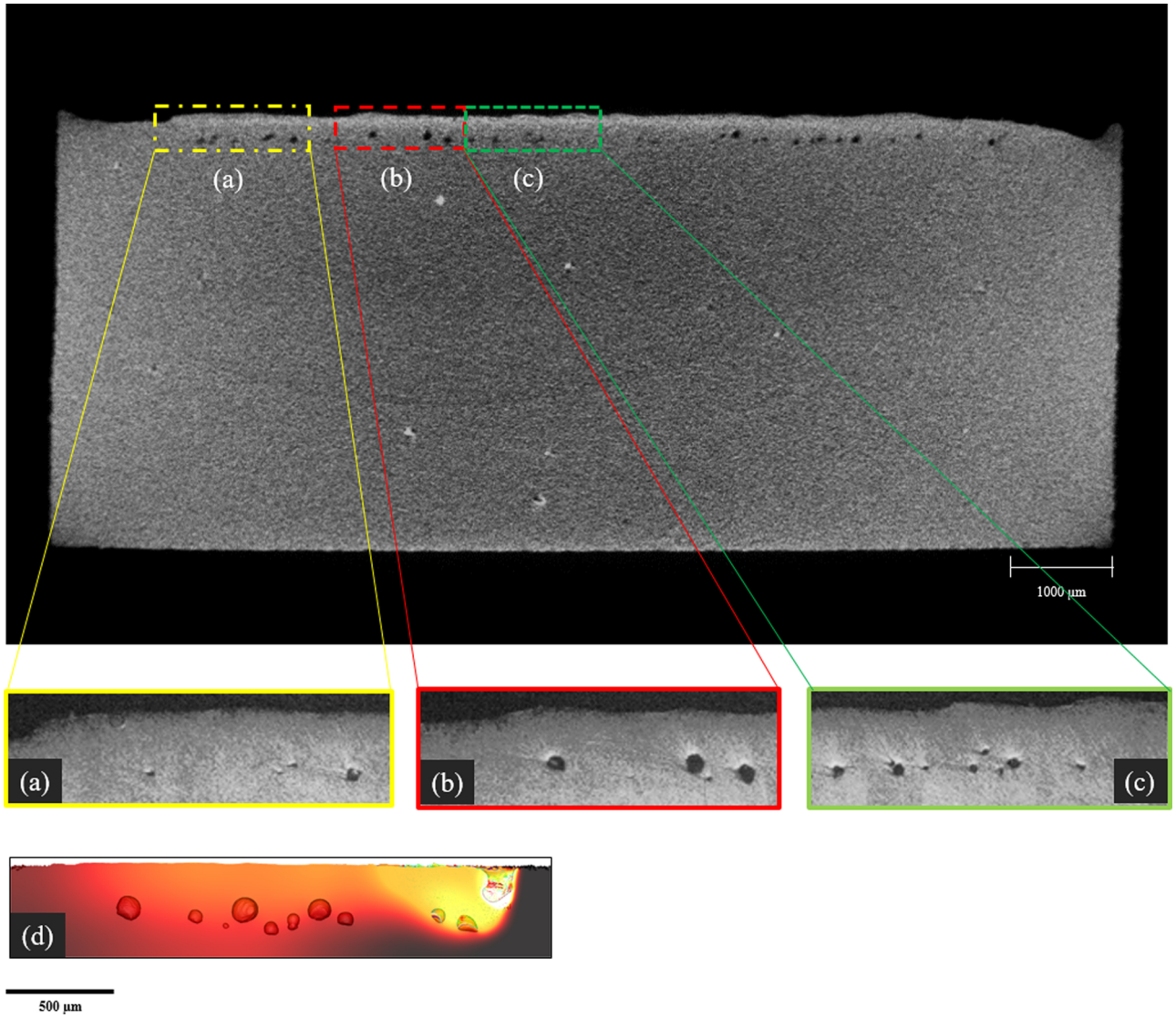

Fig. 16. X-CT scan image of the first line track. (a)–(c) are the corresponding optical images made for half of the first track for clarification. (d) Shows the results from the numerical model.

3.4. Comparison with experiments

As mentioned in Section 2, six single track lines are made with the same process parameters as listed in Table 1, all leading to the keyhole regime along with formation of porosities. Fig. 15(a)–(d) show when and where the porosities are formed during this L-PBF process.

It is observed from Fig. 15(b) that a relatively large pore is formed at the back of the melt pool. Also the floating pore seen in Fig. 15(b) as well as in Fig. 10(f) indicated by the black dashed line, escaped the free surface of the fluid at t = 3 ms, see Fig. 15(c). Moreover, different pores with various sizes and shapes are observed in Fig. 15(c) and (d). According to Fig. 15(d), the pores are formed at different depths and different lengths as well, which highlights the highly-stochastic nature of the unstable keyhole regime. The observed relative non-uniformity of keyhole-induced porosity distribution in Fig. 15 is also reported in the laser welding processes [12,29].

Fig. 16 shows an X-CT image of the first single track and (a)-(c) are its associated zoomed-in optical images for clarification. The sample has been ground and polished with oxide polishing suspensions and has been etched with Kroll's reagent, prior to the optical images. Fig. 16(d) shows the cross-section of the numerical model along with the temperature contours at the end of the process. It is observed that the depth, shape and size of the porosities are in very good agreement with the experimental optical images as well as the X-CT images. Furthermore, image analysis has been performed on the optical microscopic images to find the depth, size and distribution of the keyhole-induced porosity for the P170 case. Fig. 17 shows the numerical and experimental data regarding the porosity distribution.

The diameter shown in Fig. 17 is the diameter of a circle which is circumscribed to a pore's outer boundary. The average data for the measurements are given in Table 3 for both experiments and the model.

According to Fig. 17 and the data given in Table 3, the model slightly overestimates the size of porosity, compared to the experiments. The reason behind this difference might be due to the fact that the cutting process and its subsequent polishing, grinding and etching was not exactly done at the center of the pores, where they are supposed to have their largest profile. Moreover, there is a very good agreement in the average depth of the pores and the melt pool, according to Table 3.

In order to ensure the repeatability of the process conditions, X-CT

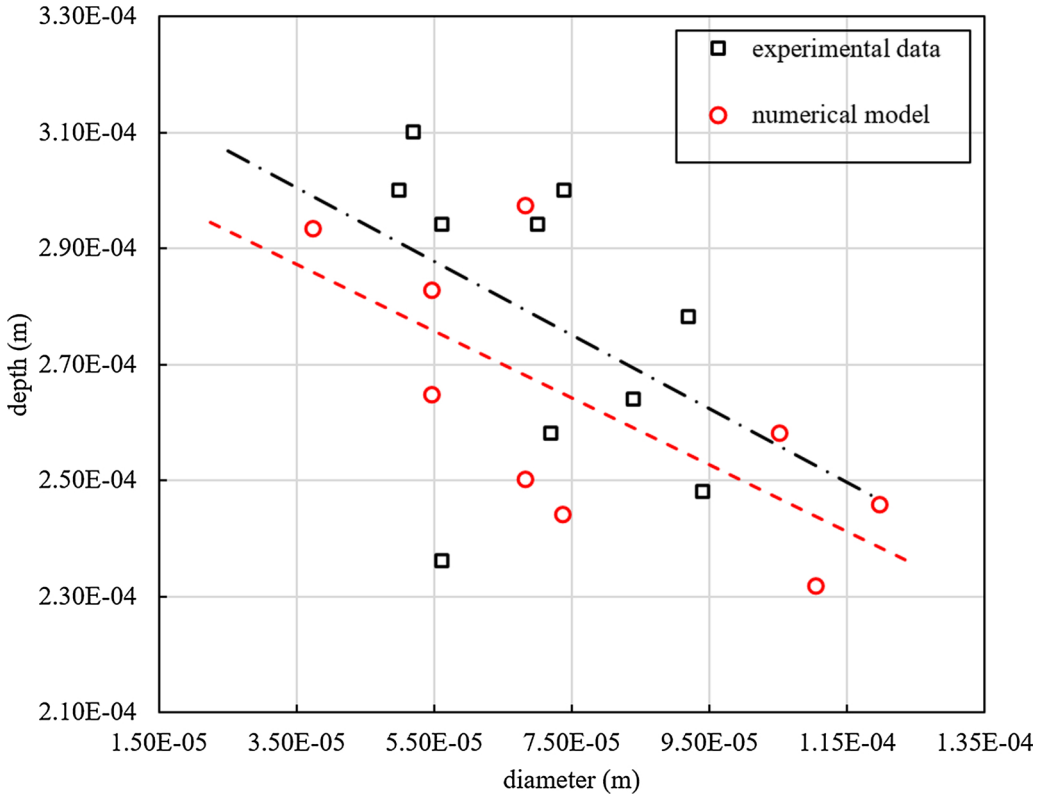

Fig. 17. Plot of depth versus diameter of porosities derived from experiments and the model for the P170 case.

Table 3
Averaged experimental and numerical data regarding size and shape of pores and the melt pool.

	Porosity		Melt pool	
	Average diameter (μm)	Average depth (μm)	Average width (μm)	Average depth (μm)
FVM model	77.01	253.21	104.71	323.47
Experiments	70.00	273.94	115.18	322.00
Error %	10.01	7.57	9.09	0.46

images of all six tracks are made and presented in Fig. 18(a)–(f). It is evident, that the pores are found to be located at the same depth and be of similar relative size/shape. Also, based on Fig. 18, one can observe the random distribution of the pores along the x-direction (parallel to the laser path), which is because of the stochastic nature of the keyhole regime. Moreover, one can notice the relatively uniform distribution of pores in the z direction as well as in the depth of the sample in Fig. 18(a)–(f), along the scanning lines. This indicates that the depth of the melt pool will become relatively constant during the process. However, as also shown in the present work, the depression zone, or the so-called keyhole, can vary rapidly within the melt pool [47]. Consequently, the pore distribution in the x direction will not be as uniform as in the z direction, in which a very good agreement is found between simulations and experiments, see Figs. 15 and 18.

A snapshot of the top surface of the model is shown and compared with experimental measurements carried out with a Keyence VHX-6000 digital 3D microscope in Fig. 19. As seen, the predicted remolten zone by the model is found to be in very good agreement with the experiments as well. The width of the melted zone is approximately 120 μm in both cases, based on Fig. 19.

4. Conclusion

In this work, a combined numerical and experimental investigation is carried out to study the formation of keyhole and keyhole-induced porosities during single track L-PBF of a Ti6Al4V alloy. For this purpose, a multiphysics numerical model has been developed with the inclusion of free surface flow, phase change/evaporation, melting/solidification, etc. The model is based on the FVM framework in the commercial software Flow-3D and to better simulate the laser-material interaction during the keyhole regime of L-PBF, multiple reflection along with the ray-tracing method are implemented. To further increase the predictive power of the numerical model, Fresnel absorption is also implemented and coupled with the ray-tracing method. It is demonstrated that the keyhole is intrinsically unstable and the transition from the stable shallow-depth melt pool to the keyhole regime is a result of a chain of multiple interconnected physical phenomena. Furthermore, a thorough investigation is carried out as regards the mechanisms of evolution and formation of the keyhole pores. It is shown that the pores are mostly formed due to occurrence of local cold zones with higher surface tension and insignificant recoil pressure. Moreover, it is demonstrated that the pores might float and escape the free surface of the liquid metal, coalesce with other pores and enlarge or even merge with the wake of the keyhole and disappear. A parametric study is carried out to assess the effect of varying laser power on heat and fluid flow conditions along with melt pool morphology. It is shown that exceeding a certain threshold of input power, a keyhole is formed. The nominal absorptivity is also calculated and it is found that it highly increases as the melt pool reaches the keyhole regime, due to better heat transfer caused by ray-entrapment. Additionally, an X-CT analysis was performed to study the keyhole-induced pores characteristics. Finally, it was shown that the predicted pore size/shape/depth are in very good agreement with both optical microscopic images and the previously

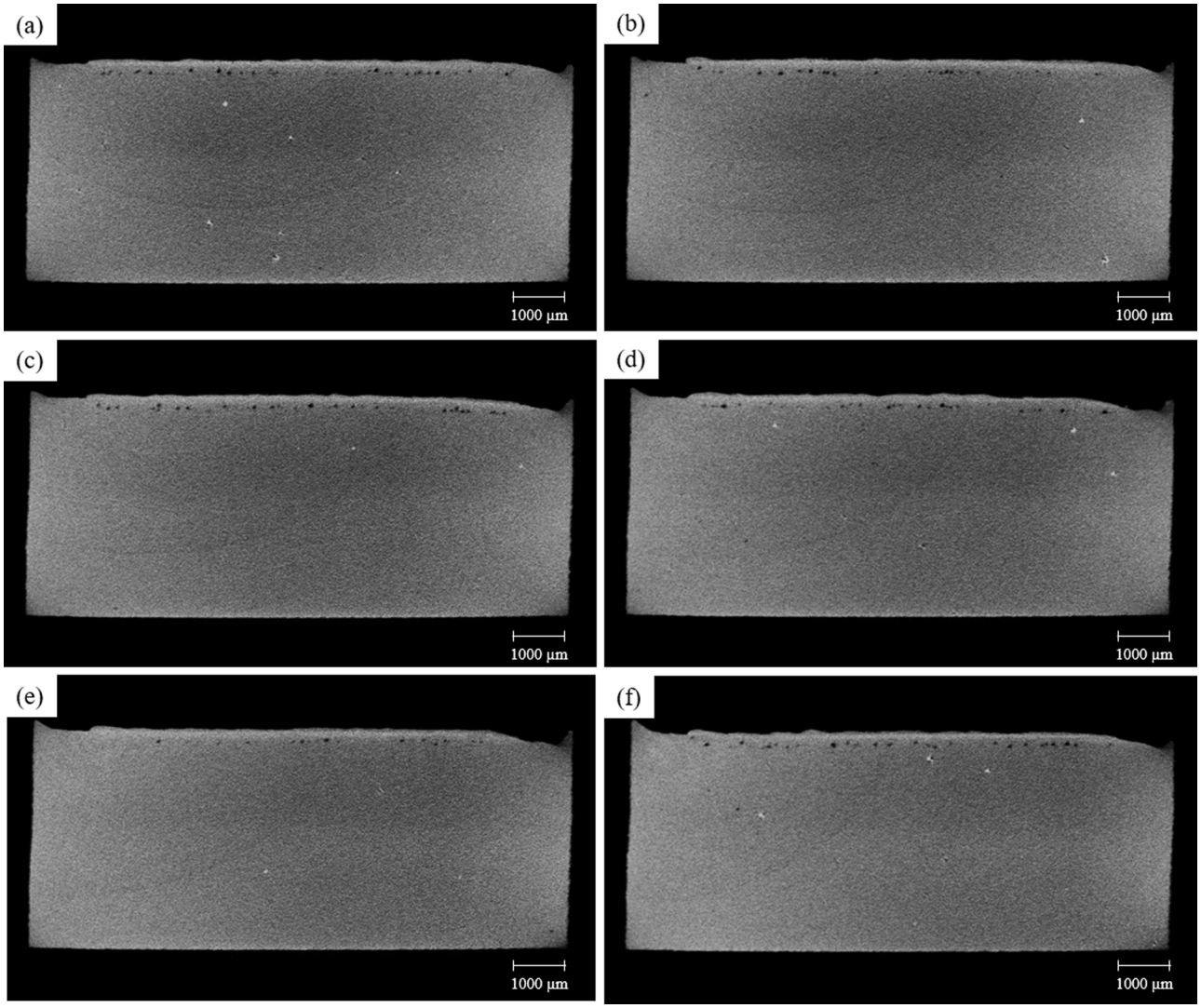

Fig. 18. X-CT images of samples for: (a) track 1, (b) track 2, (c) track 3, (d) track 4, (e) track 5 and (f) track 6.

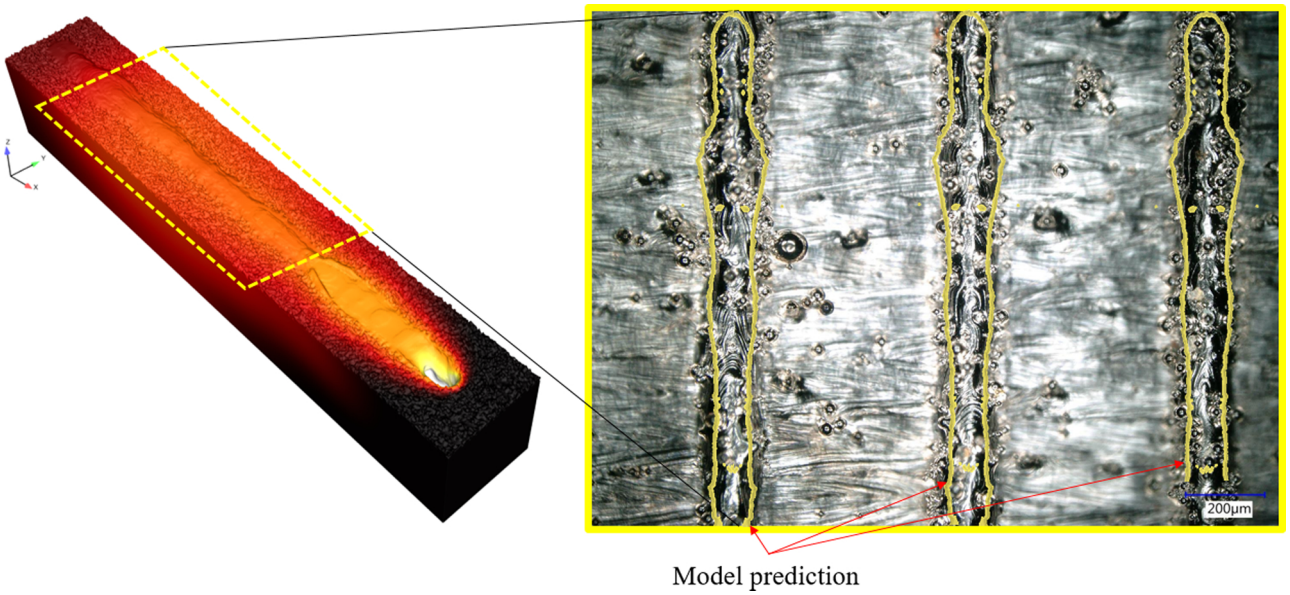

Fig. 19. (left) Full 3D view of the computational domain at the end of the process. (right) Comparison between the predicted top melt pool's resolidified surface indicated by the colored borders and experiments.

mentioned X-CT images. Moreover, the morphology of the top surface as predicted by the numerical model is compared with 3D-digital microscopic images of the samples and this showed very good agreement as well.

Declaration of Competing Interest

The authors have no conflicts of interest to declare.

Acknowledgment

This work has received funding from the European Union Horizon 2020 Marie Skłodowska_Curie ITN PAMˆ2 project under grant agreement number [721383].

References

[1] T. DebRoy, et al., Additive manufacturing of metallic components – process, structure and properties, Prog. Mater. Sci. 92 (2018) 112–224.
[2] V. Bhavar, P. Kattire, V. Patil, S. Khot, K. Gujar, R. Singh, A Review on Powder Bed Fusion Technology of Metal Additive Manufacturing, no. September (2014).
[3] M. Jamshidinia, A. Sadek, W. Wang, Additive manufacturing of steel alloys using laser powder-bed fusion, Adv Mater Process 173 (1) (2015) 4–20 K. S..
[4] M. Bayat, S. Mohanty, J. Hattel, Numerical modelling and parametric study of grain morphology and resultant mechanical properties from selective laser melting process of Ti6Al4V, Eu Spen' S 18 Th International Conference &, June, 2018 vol. 1.
[5] I. Yadroitsev, L. Thivillon, P. Bertrand, I. Smurov, Strategy of manufacturing components with designed internal structure by selective laser melting of metallic powder, Appl. Surf. Sci. 254 (4) (2007) 980–983.
[6] T. Vilaro, C. Colin, J.D. Bartout, As-fabricated and heat-treated microstructures of the Ti-6Al-4V alloy processed by selective laser melting, Metall. Mater. Trans. A Phys. Metall. Mater. Sci. 42 (10) (2011) 3190–3199.
[7] M. Bayat, D. De Baere, S. Mohanty, J. Hattel, Multi-scale multiphysics simulation of metal L-PBF AM process and subsequent mechanical analysis, The 12th International Seminar "Numerical Analysis of Weldability (2018).
[8] H. Gong, K. Rafi, H. Gu, T. Starr, B. Stucker, Analysis of defect generation in Ti-6Al-4V parts made using powder bed fusion additive manufacturing processes, Addit. Manuf. 1 (2014) 87–98.
[9] P. Edwards, M. Ramulu, Fatigue performance evaluation of selective laser melted Ti-6Al-4V, Mater. Sci. Eng. A 598 (2014) 327–337.
[10] C. Li, C.H. Fu, Y.B. Guo, F.Z. Fang, A multiscale modeling approach for fast prediction of part distortion in selective laser melting, J. Mater. Process. Technol. 229 (2015) 703–712.
[11] C. Bruna-Rosso, A.G. Demir, B. Previtali, Selective laser melting finite element modeling: validation with high-speed imaging and lack of fusion defects prediction, Mater. Des. 156 (2018) 143–153.
[12] W.E. King, et al., Observation of keyhole-mode laser melting in laser powder-bed fusion additive manufacturing, J. Mater. Process. Technol. 214 (12) (2014) 2915–2925.
[13] N.T. Aboulkhair, N.M. Everitt, I. Ashcroft, C. Tuck, Reducing porosity in AlSi10Mg parts processed by selective laser melting, Addit. Manuf. 1 (2014) 77–86.
[14] C. Zhao, et al., Real-time monitoring of laser powder bed fusion process using high-speed X-ray imaging and diffraction, Sci. Rep. 7 (1) (2017) 1–11.
[15] L.J. Zhang, J.X. Zhang, A. Gumenyuk, M. Rethmeier, S.J. Na, Numerical simulation of full penetration laser welding of thick steel plate with high power high brightness laser, J. Mater. Process. Technol. 214 (8) (2014) 1710–1720.
[16] P.A. Hooper, Melt pool temperature and cooling rates in laser powder bed fusion, Addit. Manuf. 22 (2018) 548–559.
[17] S.A. Khairallah, A. Anderson, Journal of Materials Processing Technology Mesoscopic simulation model of selective laser melting of stainless steel powder, J. Mater. Process. Tech. 214 (11) (2014) 2627–2636.
[18] S. Shrestha, K. Chou, Mesoscopic simulation model to predict temperature distribution and melt Pool size during selective laser scanning, ASME 2018 13th International Manufacturing Science and Engineering Conference (2018) January.
[19] M. Bayat, S. Mohanty, J.H. Hattel, A systematic investigation of the effects of process parameters on heat and fluid flow and metallurgical conditions during laser-based powder bed fusion of Ti6Al4V alloy, Int. J. Heat Mass Transf. 139 (2019) 213–230.
[20] S.A. Khairallah, A.T. Anderson, A. Rubenchik, W.E. King, Laser powder-bed fusion additive manufacturing: physics of complex melt flow and formation mechanisms of pores, spatter, and denudation zones, Acta Mater. 108 (2016) 36–45.
[21] Y.S. Lee, W. Zhang, Modeling of heat transfer, fluid flow and solidification microstructure of nickel-base superalloy fabricated by laser powder bed fusion, Addit. Manuf. 12 (2016) 178–188.
[22] C. Qiu, C. Panwisawas, M. Ward, H.C. Basoalto, J.W. Brooks, M.M. Attallah, On the role of melt flow into the surface structure and porosity development during selective laser melting, Acta Mater. 96 (2015) 72–79.
[23] K.H. Leitz, et al., Fundamental analysis of the influence of powder characteristics in Selective Laser Melting of molybdenum based on a multi-physical simulation model, Int. J. Refract. Met. Hard Mater. 72 (October 2017) (2018) 1–8.
[24] M.J. Matthews, G. Guss, S.A. Khairallah, A.M. Rubenchik, P.J. Depond, W.E. King, Denudation of metal powder layers in laser powder bed fusion processes, Acta Mater. 114 (2016) 33–42.
[25] Y.C. Wu, et al., Numerical modeling of melt-pool behavior in selective laser melting with random powder distribution and experimental validation, J. Mater. Process. Technol. 254 (July 2017) (2018) 72–78.
[26] M. Bayat, S. Mohanty, J.H. Hattel, Multiphysics modelling of lack-of-fusion voids formation and evolution in IN718 made by multi-track/multi-layer L-PBF, Int. J. Heat Mass Transf. 139 (2019) 95–114.
[27] J.L. Tan, C. Tang, C.H. Wong, A Computational Study on Porosity Evolution in Parts Produced by Selective Laser Melting, Metall. Mater. Trans. A Phys. Metall. Mater. Sci. 49 (8) (2018) 3663–3673.
[28] C. Tang, J.L. Tan, C.H. Wong, A numerical investigation on the physical mechanisms of single track defects in selective laser melting, Int. J. Heat Mass Transf. 126 (2018) 957–968.
[29] C. Panwisawas, et al., Keyhole formation and thermal fluid flow-induced porosity during laser fusion welding in titanium alloys: experimental and modelling, Acta Mater. 126 (2017) 251–263.
[30] I. Choquet, R.P. Turner, J.W. Brooks, H.C. Basoalto, C. Panwisawas, Y. Sovani, Modelling of thermal fluid dynamics for fusion welding, J. Mater. Process. Technol. 252 (April 2017) (2017) 176–182.
[31] A.A. Martin, et al., Ultrafast dynamics of laser-metal interactions in additive manufacturing alloys captured by in situ X-ray imaging, Mater. Today Adv. 1 (2019) 100002.
[32] R. Cunningham, et al., Keyhole threshold and morphology in laser melting revealed by ultrahigh-speed x-ray imaging, Science (80-.) 363 (6429) (2019) 849–852.
[33] J.H. Cho, S.J. Na, Implementation of real-time multiple reflection and Fresnel absorption of laser beam in keyhole, J. Phys. D Appl. Phys. 39 (24) (2006) 5372–5378.
[34] H.M. Deylami, N. Amanifard, S.S. Hosseininezhad, F. Dolati, Numerical investigation of the wake flow control past a circular cylinder with Electrohydrodynamic actuator, Eur. J. Mech. B/Fluids 66 (2017) 71–80.
[35] D. De Baere, M. Bayat, S. Mohanty, J. Hattel, Thermo-fluid-metallurgical modelling of the selective laser melting process chain, Procedia Cirp 74 (2018) 87–91.
[36] H.C. Tran, Y.L. Lo, Heat transfer simulations of selective laser melting process based on volumetric heat source with powder size consideration, J. Mater. Process. Technol. 255 (May 2017) (2018) 411–425.
[37] A. Saleem, S. Farooq, I.A. Karimi, R. Banerjee, A CFD simulation study of boiling mechanism and BOG generation in a full-scale LNG storage tank, Comput. Chem. Eng. 115 (2018) 112–120.
[38] R. Lin, H. ping Wang, F. Lu, J. Solomon, B.E. Carlson, Numerical study of keyhole dynamics and keyhole-induced porosity formation in remote laser welding of Al alloys, Int. J. Heat Mass Transf. 108 (2017) 244–256.
[39] W. Tan, N.S. Bailey, Y.C. Shin, Investigation of keyhole plume and molten pool based on a three-dimensional dynamic model with sharp interface formulation, J. Phys. D Appl. Phys. 46 (5) (2013).
[40] A. Thanki, W. Dewulf, A. Witvrouw, S. Yang, Study of keyhole-porosities in selective laser melting using X-ray computed tomography, iCT19 (January) (2019).
[41] W. Yan, et al., Meso-scale modeling of multiple-layer fabrication process in Selective Electron beam Melting: Inter-layer/track voids formation, Mater. Des. 141 (2018) 210–219.
[42] M. Gharbi, et al., Influence of various process conditions on surface finishes induced by the direct metal deposition laser technique on a Ti-6Al-4V alloy, J. Mater. Process. Technol. 213 (5) (2013) 791–800.
[43] T. Mukherjee, H.L. Wei, A. De, T. DebRoy, Heat and fluid flow in additive manufacturing – part II: powder bed fusion of stainless steel, and titanium, nickel and aluminum base alloys, Comput. Mater. Sci. 150 (February) (2018) 369–380.
[44] L. Huang, X. Hua, D. Wu, F. Li, Numerical study of keyhole instability and porosity formation mechanism in laser welding of aluminum alloy and steel, J. Mater. Process. Technol. 252 (October 2017) (2018) 421–431.
[45] X. Li, F. Lu, H. Cui, X. Tang, Y. Wu, Numerical modeling on the formation process of keyhole-induced porosity for laser welding steel with T-joint, Int. J. Adv. Manuf. Technol. 72 (1–4) (2014) 241–254.
[46] I. Kawaguchi, S. Tsukamoto, H. Honda, G. Arakane, Power modulation in deep penetration laser welding-optimization of frequency and waveform to prevent the porosity, In International Congress on Applications of Lasers & Electro-Optics, (2003) p. 1006.
[47] H. Zhao, W. Niu, B. Zhang, Y. Lei, M. Kodama, T. Ishide, Modelling of keyhole dynamics and porosity formation considering the adaptive keyhole shape and three-phase coupling during deep-penetration laser welding, J. Phys. D Appl. Phys. 44 (48) (2011).
[48] T. Qi, H. Zhu, H. Zhang, J. Yin, L. Ke, X. Zeng, Selective laser melting of Al7050 powder: melting mode transition and comparison of the characteristics between the keyhole and conduction mode, Mater. Des. 135 (2017) 257–266.
[49] G. Vastola, Q.X. Pei, Y.W. Zhang, Predictive model for porosity in powder-bed fusion additive manufacturing at high beam energy regime, Addit. Manuf. 22 (May) (2018) 817–822.
[50] J. Trapp, A.M. Rubenchik, G. Guss, M.J. Matthews, In situ absorptivity measurements of metallic powders during laser powder-bed fusion additive manufacturing, Appl. Mater. Today 9 (2017) 341–349.